2015

Large Scene SAR Image Formation

LeRoy A. Gorham

Wright State University

Repository Citation

Gorham, LeRoy A., "Large Scene SAR Image Formation" (2015). *Browse all Theses and Dissertations*. 1606.
https://corescholar.libraries.wright.edu/etd_all/1606

LARGE SCENE SAR IMAGE FORMATION

A dissertation submitted in partial fulfillment
of the requirements for the degree of
Doctor of Philosophy

by

LEROY A. GORHAM
A.S., Hudson Valley Community College, 1995
B.S., Worcester Polytechnic Institute, 1998
M.S., Northeastern University, 2002

2015
Wright State University

WRIGHT STATE UNIVERSITY

GRADUATE SCHOOL

November 19, 2015

I HEREBY RECOMMEND THAT THE DISSERTATION PREPARED UNDER MY SUPERVISION BY LeRoy A. Gorham ENTITLED Large Scene SAR Image Formation BE ACCEPTED IN PARTIAL FULFILLMENT OF THE REQUIREMENTS FOR THE DEGREE OF Doctor of Philosophy

Brian D. Rigling, Ph.D.
Dissertation Director

Ramana V. Grandhi, Ph.D.
Director, Ph.D. in Engineering Program

Robert E. W. Fyffe, Ph.D.
Vice President for Research and
Dean of the Graduate School

Committee on
Final Examination

Brian D. Rigling, Ph.D.

Fred D. Garber, Ph.D.

John M. Emmert, Ph.D.

Michael Bryant, Ph.D.

Randolph L. Moses, Ph.D.

ABSTRACT

Gorham, LeRoy A., Ph.D., Engineering Ph.D. Program, Department of Electrical Engineering, Wright State University, 2015. *Large Scene SAR Image Formation.*

With new advances in digital signal processing technology, Synthetic Aperture Radar (SAR) systems are capable of collecting high resolution data over very large scenes. Well known image formation algorithms such as the polar format algorithm (PFA) create image artifacts in large images due to phase errors introduced by the algorithm. In this dissertation, we analyze the nature of these artifacts by comparing PFA to an exact imaging algorithm, the backprojection algorithm (BPA). First, we perform a novel phase error analysis by decomposing the PFA phase errors into constant, linear, and quadratic terms for arbitrary flight paths. Second, we utilize the expressions for PFA phase errors to accurately determine scene size limitations, with examples provided for linear and circular flight paths. Third, we develop a novel adaptation of PFA which corrects a significant amount of the phase errors, thereby greatly increasing the allowable scene size of the algorithm. These results are demonstrated using both simulated and measured SAR data sets.

Abbreviations and Symbols

Throughout this dissertation numerous abbreviations and symbols are used. While the definitions can be found in surrounding text, this section provides a quick reference.

List of Abbreviations

AFRL	Air Force Research Laboratory
BPA	Backprojection Algorithm
CAT	Computer-Aided Tomography
CZT	Chirp z-Transform
DIFSAR	Differential Interferometric Synthetic Aperture Radar
DBS	Doppler Beam Sharpening
ERIM	Environmental Research Institute of Michigan
FBPA	Fast Backprojection Algorithm
FFT	Fast Fourier Transform
FPFBPA	Factorised Polar Format Backprojection Algorithm
FPGA	Field Programmable Gate-Array
GPU	Graphics Processing Units
HPC	High Performance Computing
IFP	Image Formation Processor
IFSAR	Interferometric Synthetic Aperture Radar
LFM	Linear Frequency Modulated
MAP	Maximum-a-Posteriori
MTRC	Motion Through Resolution Cells
NuFFT	Non-uniform Fast Fourier Transform
PFA	Polar Format Algorithm
PRF	Pulse Repetition Frequency
QPE	Quadratic Phase Error
RMA	Range Migration Algorithm
SAR	Synthetic Aperture Radar
SNR	Signal-to-Noise Ratio
SVPF	Space-Variant Post-Filtering
USFFT	Unequally-Spaced Fast Fourier Transform

List of Symbols

A	Constant that appears in phase terms
B	Scattering coefficient of the target
f_k	Frequency of the k^{th} sample within a pulse
(f_x,f_y)	Spatial frequency in range and cross range, respectively
$I(\bar{p})$	Matched filter response of the point target
k_0	Center wavenumber (corresponding to center wavelength)
K	Number of frequency samples per pulse

L_a	Length of synthetic aperture (linear flight path)
N_p	Number of pulses used to form SAR image
(N_x,N_y)	Size of polar format grid in spatial frequency
$\bar{p}$	Location of stationary point target
r_a	Distance from the antenna phase center to scene center
r_{a0}	Distance from the center of the synthetic aperture to scene center
r_p	Distance from the antenna phase center to the target
r_{p0}	Distance from the center of the synthetic aperture to the target
r_{max}	Allowable scene radius for PFA
$s(x, y)$	SAR image (no distortion, good focus)
$s(\tilde{x}, f_y)$	Range-compressed PFA image after defocus correction
$s(\tilde{x}, \tilde{y})$	SAR image (distortion, good focus)
$\tilde{s}(x, y)$	SAR image (no distortion, defocus)
$\tilde{s}(\tilde{x}, f_y)$	Defocused range-compressed PFA image
$\tilde{s}(\tilde{x}, \tilde{y})$	SAR image (distortion, defocus)
$S(f_k, \tau_n)$	Phase history data
$S(f_x, f_y)$	Polar formatted phase history data
t	Time during synthetic aperture, defined as $t \in [-1, 1]$
(x, y, z)	Cartesian coordinates of stationary point target
$(\tilde{x}, \tilde{y}, \tilde{z})$	Cartesian coordinates of stationary point target in distorted PFA image
$\hat{x}$	x-coordinate of target location used in QPE correction
(x_a, y_a, z_a)	Cartesian coordinates of antenna phase center
$(x_0{}', y_0{}')$	Slant plane target location given notation of [1]
x_{a0}	Ground range from scene center to antenna phase center
y_0	Flight path offset (squinted flight path)
X_1	Spatial frequency coordinate given notation of [1]
$\underline{\gamma}$	Antenna phase center location
ΔR	Differential range to the point target
$\Delta \hat{R}$	Far-field approximation of differential range used by PFA
θ_a	Elevation angle of antenna phase center
θ_s	Squint angle of antenna phase center
λ	Center wavelength of radar pulse
ρ_a	Azimuth resolution
τ_n	Time of the n^{th} pulse
Φ	Exact target phase
(Φ_0,Φ_1,Φ_2)	Exact constant, linear, and quadratic phase terms
$\hat{\Phi}$	Approximated target phase compensated by PFA
$(\hat{\Phi}_0,\hat{\Phi}_1,\hat{\Phi}_2)$	Approximated constant, linear, and quadratic phase terms
$\bar{\Phi}$	Residual target phase error after PFA
$(\bar{\Phi}_0,\bar{\Phi}_1,\bar{\Phi}_2)$	Residual constant, linear, and quadratic phase error terms
Φ_c	QPE correction
Φ_r	Residual QPE after fast correction algorithm
ψ_a	Azimuth angle of antenna phase center
ψ_t	Integration angle of synthetic aperture (circular flight path)

Contents

List of Figures

I can do all this through him who gives me strength.

–Apostle Paul (Phil 4:13, NIV)

Chapter 1

Introduction

Synthetic Aperture Radar (SAR) is a well-known remote sensing technique with applications in commercial, scientific and military communities. SAR provides several unique capabilities, among them the ability to image at night as well as during the day, and the ability to image through clouds and foliage depending on the wavelength [2]. A famous use of SAR was the mapping of the entire planet Venus [3] in the early 1990s. Venus is covered by a dense, opaque cloud layer, which does not allow imaging at optical wavelengths. Radar waveforms centered at 2.4 GHz were able to penetrate the clouds, and a relatively simple image formation algorithm [4] was used as the SAR resolution was very coarse (> 100 m).

It is generally accepted that the principles of SAR were first developed by Carl Wiley of Goodyear Aircraft Corporation in June 1951 [5]. Early SAR systems used optical processing [6] for image formation, and an excellent description of an optical processor is provided by Dr. William Brown in 1969 [7]. Modern SAR systems utilize digital processing [8], and take advantage of commercial advancements in processing power and storage. A good example of this is the implementation of SAR processing on Graphics Processing Units (GPU) [9] which were originally designed for the gaming industry.

SAR requires specialized algorithms, called Image Formation Processors (IFPs), to convert radar returns into images. A myriad of IFPs have been developed, and a thorough review of SAR imaging algorithms is provided in Section 2.1.1. In this dissertation, we focus on two well-known IFP's: Backprojection Algorithm (BPA) [10, 11] and Polar Format Algorithm (PFA) [1, 12]. In [13], BPA was derived from a matched filter, which maximizes signal-to-noise ratio (SNR) [14], under ideal conditions (i.e., an isolated isotropic point target in white Gaussian noise). BPA is ideal in that the algorithm does not introduce any image artifacts due to phase errors. However, the algorithm is slow, requiring $\mathcal{O}(N^3)$ operations [13] for an $N \times N$ pixel image with critical sampling. In contrast, PFA is significantly faster than BPA, with the tradeoff that the matched filter is approximated, thus resulting in image artifacts such as distortion and defocus for large scene sizes. PFA approximates the curved wavefront of the radar wave propagation with a planar wavefront which allows the use of Fast Fourier Transforms (FFTs) that result in a more efficient implementation on a variety of processors. A typical PFA implementation requires $\mathcal{O}(N^2 \log N)$ operations for an $N \times N$ pixel SAR image.

1.1 Motivation

Wide area, staring SAR sensors [15–17] have been shown to offer unique exploitation capabilities, such as the detection of slow moving targets [18] and improved vehicle identification [19–22]. However, these capabilities come at the cost of significantly increasing the computational burden of the IFP. Wide area SAR images typically exceed the scene size limitations of fast image formation algorithms, such as PFA, which result in image artifacts such as distortion and defocus.

There are three approaches to solving the large image formation problem. One is the use of exact algorithms like BPA in a High Performance Computing (HPC) environment [9, 23, 24]. BPA is an embarrassingly parallel algorithm, since the calculation of every pixel is an independent process without any dependency on other pixels. This makes it relatively easy to implement BPA in a parallel computing environment. However, there are many logistical problems with this approach that require clever computer science techniques to solve [25]. Through use of BPA, SAR images will have no phase error induced by the IFP, resulting in images that have no distortion and are well focused.

A second approach is to use fast image formation algorithms (such as PFA) by first dividing the image into small enough patches such that image artifacts are minimized. The process of subdividing the image into patches before actually forming the image is called Digital Spotlighting [26]. This approach is analyzed in detail in [27].

A third approach is to use fast image formation algorithms, but instead of creating smaller image patches to minimize image artifacts, corrections are applied after image formation [28]. If the flight path is known, the residual phase errors after image formation are deterministic and appropriate correction filters can be constructed. However, in general, these phase errors vary spatially across the image, and a brute force correction of each pixel is more computationally expensive than BPA.

This dissertation improves upon the third approach by providing a faster algorithm for applying these corrections. Specifically, a novel variant of PFA is developed that maximizes the efficiency of the post-image corrections.

1.2 Contributions

This dissertation includes three significant contributions, culminating in a new computationally efficient image formation algorithm for circular flight paths that corrects for distortion and defocus artifacts. The three contributions are detailed in the following subsections.

1.2.1 Improved PFA Phase Error Analysis

This disseration extends previous work in phase error analysis by using a novel technique for decomposing PFA phase errors into constant, linear, and quadratic terms for arbitrary flight paths. A comprehensive literature review of phase error analysis is provided in Section 2.1.2.

In order to analyze the image artifacts resulting from PFA in large scenes, the residual phase error is analyzed based on the approximations used in PFA. One of the biggest drivers of computational complexity in BPA is that the exact range is calculated for every pixel in the image for every sensor position along the flight path. Typically, this range is calculated using the Euclidean distance in the sensor coordinate system, and this range is used to calculate the exact phase required to matched filter the SAR phase history data. In PFA, the range is not explicitly calculated in this manner. Instead, a far-field approximation is used which gives a linear estimate of the phase, and the matched filter is performed using 2-D FFTs.

Using a Taylor Expansion in the image coordinates [29], it was shown that this linear estimate of the phase is equivalent to an approximation of the range calculation. By analyzing the second order terms of the Taylor Expansion, the residual quadratic phase error (QPE) was calculated for a linear flight path scenario. Other analyses [30, 31] performed the Taylor Expansion in the frequency domain instead of image coordinates.

This dissertation extends the previous work [29] by performing the Taylor Expansion in the temporal dimension along the flight path. This allows for more accurate isolation of the constant, linear and quadratic phase error terms for any arbitrary flight path. The Taylor Expansion is used to derive a closed-form analytic expression for constant, linear and quadratic phase errors.

The PFA phase error analysis is described in detail in Chapter 3. This analysis is also included in a journal paper [32] which was accepted for publication in 2015. Preliminary results were also published in a 2013 letter [33].

1.2.2 Derivation of Accurate Scene Size Limitations

The second significant contribution is the derivation of accurate scene size limitations for arbitrary flight paths. A comprehensive literature review of previous work in this area is provided in Section 2.1.3. A critical component of this derivation is that we include the distortion correction of linear phase error as part of the QPE analysis. In Chapter 4, the expression for the residual QPE is given as a function of both the actual target location and the apparent (distorted) image location of the target. Including the impact of distortion when determining the region of acceptable focus is a novel contribution. Earlier works [1, 12, 29, 30, 34, 35] provide only a maximum scene diameter or radius in their analysis. In this dissertation, we determine regions of focus that are arbitrary in shape to account for all areas in the image with acceptable image focus.

In this dissertation, we use the analytic expressions described in Section 1.2.1 to derive accurate scene size limitations for arbitrary flight paths. First, the linear phase error expressions are used to solve for the distortion in the PFA images. By equating the constant and linear phase terms of BPA with the constant and linear phase terms of PFA, the exact mapping between the 3-D scene into the 2-D image is derived. This expression accounts not only for the distortion in the PFA images, but also for other SAR phenomenon such as layover [36].

Second, the QPE expressions are used to solve for the defocus in the PFA images. The difference between the quadratic phase terms of BPA and the quadratic phase terms of PFA quantifies the defocus in the PFA image. We assume that the image is well focused if the QPE is less than $\pi/2$ [29, 34]. With these expressions, we derive a closed-form solution for the region of the PFA image that is well focused. This solution is verified using point target simulations for both a circular and a linear flight path.

The derivation of accurate scene size limitations is described in detail in Chapter 4. This analysis is also included in a journal paper [32] which was accepted for publication in 2015.

1.2.3 Fast PFA Corrections for a Circular Flight Path

The third significant contribution is the development of a fast algorithm that corrects for distortion and defocus errors in PFA for a circular flight path. Since we have isolated the linear and quadratic phase error terms for any arbitrary flight path, we can use these deterministic expressions to apply corrections to the PFA image. In general, these correction terms can be applied via a complex multiplication in the phase history domain. However, the appropriate corrections vary across the image in both dimensions, and a brute force approach to applying the corrections is computationally expensive. Therefore, a fast algorithm is desired to apply these corrections.

The developed fast algorithm works in two steps. First, the defocus is corrected, and then the distortion is corrected. For the circular flight path, the QPE varies mostly with the range to the scatterer and very little with the cross range distance in the distorted PFA image coordinates. Therefore, a computationally efficient approach is to apply the same QPE correction across an entire column of pixels before the azimuth FFT step in PFA. The appropriate correction is calculated at the center pixel in every column (representing the center of the image in azimuth). This simple correction adds comparatively few computations to the imaging process, and yet it corrects a significant amount of defocus, thereby greatly increasing the focused scene size. The distortion correction is then applied by simply interpolating the distorted image to a warped grid which compensates for the constant and linear phase error terms.

In Chapter 5, the new algorithm is described in detail. The algorithm is demonstrated on point target simulations and a measured large scene dataset. Also, the increase in the focused scene size and the computational efficiency of the algorithm are quantified. This analysis is also included in a journal paper [37] which was submitted for publication to IEEE AES in 2015. A comprehensive literature review of PFA correction algorithms is provided in Section 2.1.4.

1.2.4 Published Papers Related to this Dissertation

As part of the research for this dissertation, several papers were written and submitted for publication. Initial results were published in the SPIE Algorithms for SAR Imagery Conference [13, 38–41]. In 2013, we published a paper [33] on the allowable scene sizes for PFA imaging with postfiltering. In 2014, we published a paper [27] which presented analysis of the computational cost of several SAR image formation algorithms with nonlinear flight trajectories.

Also in 2014, we wrote a paper [32] that has been accepted for publication which includes the phase error analysis and scene size limitations. The majority of this paper is included in Chapters 3 and 4. In 2015, we wrote a paper [37] that has been submitted for publication which includes the fast correction algorithm for circular flight paths. The content of this paper is included in Chapter 5.

1.3 Outline of Dissertation

In Chapter 2, we provide background material including a literature review and a description of the IFPs used in this dissertation, namely PFA and BPA. In Chapter 3, we present the improved PFA phase error analysis for arbitrary flight paths. In Chapter 4, we describe the derivation of accurate scene size limitations and give examples for linear and circular flight paths. In Chapter 5, we use the results from the phase error analysis to develop an improved fast algorithm for circular flight paths. Finally, in Chapter 6 we summarize the dissertation and offer some thoughts regarding follow-on research in this area.

1.4 Notation

In this dissertation, we define a Cartesian coordinate system where the origin corresponds to the center of the imaging scene. We also assume that the SAR operates in spotlight mode, with the origin as the motion compensation point. This means that every pulse is compensated exactly for an ideal scatterer at scene center whose received signal has constant phase [12].

We also use the imaging convention that the x-axis corresponds to the range dimension, the y-axis corresponds to the cross range dimension, and the z-axis is the vertical dimension. Any dataset can easily be transformed into these coordinates by a simple rotation. For instance, the measured dataset [42] described in Section 2.5.2 uses an East-North-Up convention. We simply rotate the coordinate system by the azimuth angle at the center of the aperture. Note that this is flipped from [1], which defines the y-axis as range and the x-axis as cross range.

The remainder of the notation is defined in Chapter 2. The image geometry and data model is described in Section 2.2 and the linear and circular flight paths are defined in Section 2.4.

Chapter 2

Background

This chapter includes background that provides context for the research described in the dissertation. Section 2.1 provides a thorough literature review. Section 2.2 describes the image geometry and data models used in the dissertation. Section 2.3 describes the two IFP algorithms used in this dissertation, namely PFA and BPA. Section 2.4 provides definitions for the linear and circular flight paths, and also calculates some derivatives that will be useful in the scene size limitation analysis. Finally, Section 2.5 describes the datasets used in the dissertation.

2.1 Literature Review

There have been numerous books written on different aspects of SAR, and several of them include significant content regarding image formation algorithms. A few popular books are [1, 2, 12, 14, 43–49]. There have also been numerous survey papers written on various subjects. Sherwin [50] provides a good history of the early developments in SAR, and Brown [7] provides a good introduction to SAR in 1969. Elachi [51] wrote a very detailed paper on spaceborne SAR systems in 1982. In 2000, Rosen [52] described SAR interferometry in detail. In 2013, Reigber [53] described recent advancements in SAR, especially as they pertain to very high resolution imaging.

2.1.1 Review of SAR Imaging Algorithms

Early SAR systems used rectangular range-Doppler processing to form images, which we would now call unfocused SAR, or Doppler Beam Sharpening (DBS) [8]. Techniques were developed [54] to account for defocusing due to target motion through resolution cells (MTRC) [12], but this technique is only practical for coarse resolution imaging.

As radar technology improved (such as the advent of stretch processing [55]), finer resolution imaging became more practical. Walker [34] related a new range-Doppler imaging algorithm, which became known as PFA. PFA is described in detail in Section 2.3.2. Doerry [56] wrote an extensive report for Sandia National Laboratories which covers the basics of PFA with an emphasis on real-time implementations. In 2008, PFA was implemented using the principle of chirp scaling [57], which used the properties of the linear frequency modulated (LFM) signal to speed up the algorithm. In 2011, PFA was modified [58] such that the plane wave assumption was replaced by a spherical wave approximation, which leads to an increased scene size for spaceborne applications.

One aspect of PFA that required significant research was the polar interpolation process. The theory for interpolating digital signals was described in detail by Crochiere and Rabiner [59] in 1981. Munson [60] provided a comparison between 2-D interpolation and separable 1-D interpolations, and he concluded that the 2-D interpolation yields only a small performance improvement over the vastly computationally efficient 1-D interpolations. The medical imaging community calls this process Gridding, and there have been several papers published [61–64] attacking this problem. In 2007, a comparison between radar and medical imaging PFA implementations was performed [39] which suggested that the methods were similar in performance. In 2012, Doerry [65] published a comprehensive paper describing the interpolation process and offered several possible solutions to the problem. In 2014, a MATLAB implementation of PFA was published [66].

There have been a few approaches that avoid the interpolation step altogether. In 2005, the unequally-spaced FFT (USFFT) [67] was applied to PFA image formation. A novel approach to the problem was offered by Wang [68], where the authors derived a specialized non-linear flight path whereby the polar interpolation is no longer necessary for image formation. In 2014, Fan [69] used a fast Gaussian grid non-uniform FFT instead of the polar interpolation with good results.

In 1983, Munson [11] applied tomographic processing that was used in medical imaging such as Computer-Aided Tomography (CAT) to the SAR reconstruction problem. The theory for reconstructing optical images from their projections was detailed by Mersereau and Oppenheim [70] in 1974 and by Stark and Woods [71] in 1981. This led to the development of BPA [10] in 1992. A distinct advantage of BPA is the ability to form SAR images as phase history is collected, pulse by pulse, and to integrate newly obtained information into the SAR image as it becomes available. BPA also allows for arbitrary imaging grids. However, BPA is computationally expensive as it requires $\mathcal{O}(N^3)$ operations for an NxN SAR image. In 1995, Jakowatz [72] extended BPA to 3-D imaging. In 1997, Cetin and Karl [73] formulated the tomographic imaging problem as a Maximum-a-Posteriori (MAP) estimation problem, which offers enhanced noise suppression.

Despite its inherent flexibility, BPA was too computationally expensive for most applications. Therefore, several approaches were pursued to speed up the algorithm while retaining the advantages of BPA. Most of these fast backprojection algorithms (FBPA) offer decreased computational complexities of $\mathcal{O}(N^{5/2})$ or $\mathcal{O}(N^2 \log N)$. In 1996, McCorkle [74] introduced a quadtree FBPA, which factorizes the phase history data into subimages. In 1999, Yegulalp [75] introduced a fast algorithm which forms subimages on a Nyquist sampled polar imaging grid using BPA (utilizing the fact that BPA can form images on any arbitrary grid), interpolates the subimages onto the desired imaging grid, and coherently sums the resultant images.

Another form of FBPA uses a technique called digital spotlighting [14, 76–78], which is a signal processing method that creates a subset of the phase history data corresponding to a subset of the image. This version of FBPA uses digital spotlighting to break apart a large

SAR phase history into a series of smaller SAR phase histories which are then processed into images using BPA. This algorithm [27] essentially trades BPA computations with digital spotlighting computations. Since digital spotlighting has computational complexities of $\mathcal{O}(N^2)$ instead of $\mathcal{O}(N^3)$, this algorithm is significantly faster. A Factorised Polar Format BPA (FPFBPA) has also been developed [79] which further reduces the computation complexity. Another version of FBPA integrates a geometrical autofocus algorithm [80] for better image focus in the presence of navigation errors.

Parallel processing techniques have been applied to SAR image formation as far back as 1990 [81]. In 2005, Buxa [82] showed a 150x speed-up of BPA using Field Programmable Gate-Array (FPGA) processors. Other implementations of BPA on FPGAs have been shown [83, 84]. In 2006, the quadtree FBPA was implemented on varying parallel processors [38] and compared with standard BPA. Recently there have been several implementations of SAR image processing on GPUs, including [23, 25, 85–87]. In 2012, SAR image formation was implemented on a low power multi-core Digital Signal Processor from Texas Instruments [88].

One imaging algorithm not addressed in this dissertation is the Range Migration Algorithm (RMA). RMA was first introduced to stripmap SAR by Rocco [89] and Cafforio [90] using techniques first developed for seismic imaging. RMA was expanded to spotlight mode SAR by Prati [91]. RMA does not make a far-field assumption as in PFA, and therefore distortion and defocus due to range curvature are not an issue. However, RMA processing requires a higher along-track sampling than PFA [12], which leads to a significant increase in the pulse repetition frequency (PRF) of the SAR system [27]. In 2014, an interpolation-free version of RMA was introduced [92] and tested on simulated data. RMA has also been implemented on FPGAs using the Non-uniform FFT (NuFFT) [93].

There have also been several papers [27, 94–100] that have compared imaging algorithms using varying criteria.

2.1.2 Phase Error Analysis of Imaging Algorithms

The use of Taylor series to analyze the phase errors in SAR imagery dates back to 1980, when Walker [34] used a 2-D Taylor series in the image domain. A comprehensive phase error analysis is given in Section 3.5 of [12], where a 2-D Taylor series expansion of the signal phase is derived. The authors state that this approach was first developed in unpublished analyses by J. Craig Dwyer at the Environmental Research Institute of Michigan (ERIM). In Section 3.7 of [12], the Taylor series analysis is used to isolate distortion and defocus due to range curvature. Fienup [101] extended this analysis for moving targets, and also provided exceptional insight into the various phase terms that arise in the analysis.

In 1986, Zeoli [102] showed that a constant velocity error causes a QPE and provided an analytic solution to the problem. Carrara [12] compared several different imaging algorithms in terms of phase errors. In his 1999 Ph.D. thesis, Doren [30] performed an extensive analysis on the planar wavefront assumption. This Taylor series was used in the frequency (k-space) domain instead of the image domain, following the methodology developed by Jakowatz [1].

In 2002, Fornaro [103] performed a phase error analysis on squinted data collected in strip-map mode and looked to correct abberations appearing in interferometric (IFSAR) and differential interferometric (DIFSAR) applications. In 2009, Xie [104] used a Taylor Expansion to analyze the signal characteristics of missile-borne SAR.

2.1.3 Scene Size Limitations

Most of the papers and books cited in Section 2.1.2 used the phase error analysis to determine scene size limitations. There is some discrepancy as to the acceptable level of QPE in a well focused image. Some sources [29, 34] cite a $\pi/2$ error is acceptable while others [1, 30] indicate a more stringent requirement of $\pi/4$.

In 2006, Doerry [35] published an extensive report for Sandia which utilized the analysis in [30] to derive scene diameter limits for a circular flight path, a linear flight path with no squint, and a linear flight path with squint. Another Sandia report [105] performed a survey of the assumptions and approximations that limit the performance of PFA.

In a series of articles [106, 107], Zhu looked at the scene size limit of PFA for moving target imaging. Another paper [108] studied how image artifacts affect target classification and developed an application-driven scene size limit.

2.1.4 Phase Error Correction Algorithms

In 1996, Berizzi [109] proposed an autofocus solution to correct for phase errors. The authors sought to estimate a higher order polynomial approximation by optimzing image contrast, but they did not state the computational cost of such an approach.

Doren and Jakowatz [28, 30, 110] derived a space-variant post-filtering (SVPF) algorithm that corrects for the range curvature effects due to PFA. Preiss [111] extended this work to show that IFSAR processing is possible using these post-filtered images. This post-filtering approach does not change the PFA in any way; it simply provides an ad-hoc method for correcting the images after image formation. In 2011 and 2012, Mao [112, 113] proposed a better filter for the SVPF which is robust to arbitrary flight paths. In 2014, Peng [114] used the SVPF in a 3-D imaging application.

In 2004, Carrara [115] proposed changing PFA by utilizing a new along-track alignment and formatting system. This algorithm modifies the SAR phase history storage format which ultimately removes range curvature effects from the final image. The authors showed that this approach is mathmematically equivalent to RMA processing.

In 2009, Fortuny-Guasch [116] proposed the use of a pseudopolar format algorithm, but this requires a linear flight path and is intended to work with stepped-frequency continuous wave radar applications. In 2011, Liu [58] proposed an algorithm based on a spherical-wave assumption rather than a planar-wave assumption. In 2015, Fan [117] proposed a PFA based on the double Chirp z-Transform (CZT).

In 2012, Linnehan [118] provided an efficient means for mitigating the range curvature effects in PFA by breaking the image up into subimages and applying the phase corrections to the phase history before PFA processing. In 2013, Horvath [33] extended the original analysis by Rigling [29] by considering the scene size increase with the application of the second order corrections provided by the Taylor Expansion.

2.2 Image Geometry and Data Model

This dissertation uses the same Cartesian coordinate system first defined in [29] and further refined in [13]. The SAR sensor travels along an arbitrary flight path, and we define that the antenna phase center has a location denoted by $\underline{\gamma}(t)$ such that

$$\underline{\gamma}(t) = [x_a(t), y_a(t), z_a(t)]^T \tag{2.1}$$

where t denotes the slow-time dimension during the imaging interval. We define all coordinates with respect to the origin of the coordinate system, which corresponds to the SAR motion compensation point. The distance from the antenna phase center to the origin is denoted as

$$r_a(t) = \|\underline{\gamma}(t)\| = \sqrt{x_a^2(t) + y_a^2(t) + z_a^2(t)}. \tag{2.2}$$

To simplify subsequent analysis without loss of generality, we define the synthetic aperture to occur in the time interval $t \in [-1, 1]$. We also define a stationary target located at

$$\underline{p} = [x, y, z]^T. \tag{2.3}$$

In general, this target can have any arbitrary motion, but in this dissertation, we will assume that the target is stationary.

At periodic intervals, the radar transmits a pulse that reflects off scatterers in the scene and some of the reflected energy is received by the radar. In a given synthetic aperture, there are N_p pulses used to form the image. The time of each pulse is denoted by the sequence $\{\tau_n | n = 1, 2, \ldots N_p\}$. Assuming dechirp-on-receive processing [55], the output of the receiver at a given time τ_n can be viewed as a sequence of frequency samples over the bandwidth of the received pulse, with a phase shift corresponding to the round-trip time to the target. There are K frequency samples per pulse, and the associated frequency values are represented by the sequence $\{f_k | k = 1, 2, \ldots K\}$.

We define the receiver output, $S(f_k, \tau_n)$, of a single isotropic point target located at $\underline{p}$ as

$$S(f_k, \tau_n) = B \exp\left(\frac{-j4\pi f_k \Delta R(\tau_n)}{c}\right), \tag{2.4}$$

where B represents the scattering coefficient of the point target along with any gains and phases from pulse transmission, propagation, and reception. The differential range of the point target is represented by

$$\Delta R(\tau_n) = r_p(\tau_n) - r_a(\tau_n) \tag{2.5}$$

where r_a is defined in (2.2) and r_p is the distance between the sensor and the target $\underline{p}$, given by

$$r_p(t) = \sqrt{[x - x_a(t)]^2 + [y - y_a(t)]^2 + [z - z_a(t)]^2}. \tag{2.6}$$

2.3 SAR Image Formation Algorithms

Digital image formation techniques generally fall into two categories. The first category consists of exact image formation algorithms, which are derived from a matched filter [119] or the projection slice theorem [11]. These approaches are typically implemented with BPA [10], which is described thoroughly in Section 2.3.1.

The second category consists of fast image formation algorithms, which use approximations to reduce the amount of computations required to form the image. Typically the quality of the images formed with fast algorithms is equivalent to the exact algorithms near the center of the image, but image artifacts appear as you get further away from the center. Therefore, fast algorithms are limited by the size of the artifact-free image. A popular fast image formation algorithm is PFA [34], which makes use of the FFT [120] for efficient computation. PFA is described throughly in Section 2.3.2.

2.3.1 Matched Filter and BPA

The material from this section was included in [13] and [32]. The most straightforward method for forming a SAR image is to perform a matched filter. From (2.4), we can build the matched filter for every pixel in the image. At every pixel location $\underline{p}$, we assume an isotropic scatterer with constant scattering coefficient, B. Therefore, the matched filter response [119], which maximizes the SNR of estimates of B at location $\underline{p}$, is given by

$$I(\underline{p}) = \frac{1}{N_p K} \sum_{n=1}^{N_p} \sum_{k=1}^{K} S(f_k, \tau_n) \exp\left(\frac{+j4\pi f_k \Delta R(\tau_n)}{c} \right). \tag{2.7}$$

To form an image using this method, (2.7) is applied for each pixel in the image. This requires calculation of the differential range, $\Delta R(\tau_n)$, for every pixel for every pulse. The algorithm has a computational complexity of $\mathcal{O}(N^4)$ for 2-D images, which makes it impractical for most applications. However, (2.7) can be more efficiently implemented using BPA.

BPA implements (2.7) to form images over a grid of pixel locations by utilizing an FFT to perform the inner summation for a uniformly spaced set of differential ranges, which are then interpolated to differential ranges corresponding to each pixel location. This requires calculation of the differential range, $\Delta R(\tau_n)$, for every pixel for every pulse. This algorithm has a computational complexity of $\mathcal{O}(N^3)$ for 2-D images, which is significantly slower than PFA for most applications. However, the resulting image is completely free of distortion and defocus, and we will use (2.7) as a reference to determine the scene size limitations of PFA. As previously mentioned in Section 2.1.1, the computational complexity of BPA can be significantly reduced by implementing one of the FBPA implementations [38, 74, 75].

2.3.2 PFA

The standard implementation of PFA uses a 2-D FFT to form the SAR image efficiently. In order to use this computationally efficient approach, a far-field assumption is made. Rigling [29] showed that the PFA matched filter kernal is defined by an estimate of the differential range, ΔR such that

$$\Delta\hat{R}(t) = \frac{-1}{r_a(t)}(x_a(t)\tilde{x} + y_a(t)\tilde{y} + z_a(t)\tilde{z}) \tag{2.8}$$

where $(\tilde{x}, \tilde{y}, \tilde{z})$ are the coordinates where a target at location (x, y, z) appears in the image.

This estimate of the differential range has the effect of approximating the curved wavefront of propagation with a planar wavefront. Implementation of PFA is explained in detail in many textbooks [1, 12], so we will simply summarize the algorithm here. In order to use a 2-D FFT to form an image, the data samples need to reside on a rectilinear grid in the spatial frequency or wavenumber domain. In a typical spotlight SAR collection, the data is collected on a polar grid, so an interpolation process is required to resample the data onto a rectilinear grid. Assuming the data has been collected on a smooth grid, 1-D interpolation filters can be used to efficiently resample the data to a rectilinear grid prior to matched filtering, with minimal errors.

Figure 2.1 shows a block diagram of PFA. The incoming phase history is denoted as $S(f_k, \tau_n)$, which is defined in (2.4). This incoming phase history data is resampled onto a rectilinear grid, first by interpolating in the fast-time (range) dimension and then by interpolating in the slow-time (cross range) dimension. The resampled data is denoted as $S(f_x, f_y)$, where f_x is the spatial frequency in the range dimension and f_y is the spatial

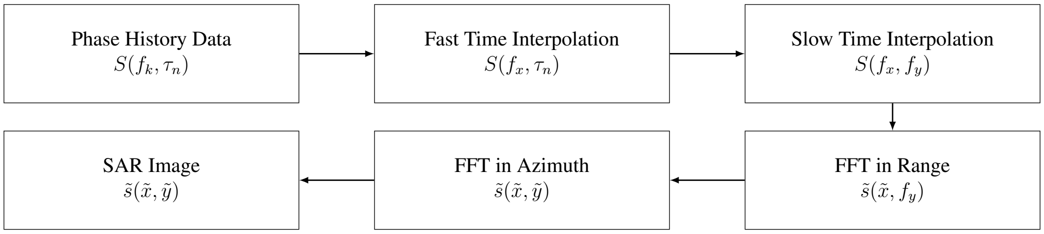

Figure 2.1: PFA block diagram

frequency in the cross range dimension.

The image is then formed by performing a 2-D FFT, which is efficiently implemented by a series of 1-D FFTs in range followed by a series of 1-D FFTs in azimuth. The result is a SAR image which contains defocus and distortion errors due to the far-field approximation. These errors are described in Chapters 3 and 4. The final image is denoted as $\tilde{s}(\tilde{x}, \tilde{y})$, where $\tilde{x}$ is the distorted range coordinate and $\tilde{y}$ is the distorted cross range coordinate. We denote this image as $\tilde{s}$ since the image also contains defocus errors. Note that in this dissertation, all images are formed in the ground plane.

2.4 Flight Path Definitions

In this dissertation, we analyze PFA phase errors for an arbitrary flight path. Then, we utilize this approach to derive specific results for a circular flight path and a linear flight path. Here, we define the geometry conventions and parameterizations of each flight path.

2.4.1 Circular Flight Path Definition

For a circular flight path, it is easier to redefine the flight path from (2.1) in spherical coordinates. We define the azimuth angle as ψ_a and the elevation angle as θ_a of the antenna phase center with the following relationships:

$$\begin{aligned}
x_a(t) &= r_a(t)\cos\theta_a(t)\cos\psi_a(t) \\
y_a(t) &= r_a(t)\cos\theta_a(t)\sin\psi_a(t) \\
z_a(t) &= r_a(t)\sin\theta_a(t).
\end{aligned} \tag{2.9}$$

An ideal circular flight path has a constant elevation, so z_a and θ_a are assumed to be constant. We also define the flight path to be centered at the origin of the coordinate system, so the distance from the antenna phase center to the origin, r_a, and the elevation angle, θ_a, are also constants. We define another constant $x_{a0} = r_a \cos\theta_a$, which is the ground range from scene center to the antenna phase center.

We define the azimuth extent of the synthetic aperture by the difference between the minimum and maximum azimuth angles, which we denote ψ_t. Since $-1 \leq t \leq 1$ is the defined time interval of the synthetic aperture, $-\psi_t/2 \leq \psi_a(t) \leq \psi_t/2$ represents the azimuth angles along the synthetic aperture. Therefore, $\psi_a(t) = (\psi_t/2)\cdot t$. We can now express the spherical coordinates as time-dependent quantities and compute their time derivatives:

$$\begin{array}{lll}
r_a(t) = r_a & \theta_a(t) = \theta_a & \psi_a(t) = \dfrac{\psi_t}{2}t \\
\dfrac{\partial r_a}{\partial t} = 0 & \dfrac{\partial \theta_a}{\partial t} = 0 & \dfrac{\partial \psi_a}{\partial t} = \dfrac{\psi_t}{2} \\
\dfrac{\partial^2 r_a}{\partial t^2} = 0 & \dfrac{\partial^2 \theta_a}{\partial t^2} = 0 & \dfrac{\partial^2 \psi_a}{\partial t^2} = 0.
\end{array} \tag{2.10}$$

We note that that a circular path can be parameterized by three variables: ψ_t, which is the size of the synthetic aperture in radians, and two of the three constants r_a, z_a and θ_a.

In the phase error analysis in Sections 3.3.2 and 4.2.1, we will need the first and second derivatives of the flight path defined in (2.9):

$$\begin{aligned} x_a\big|_{t=0} &= x_{a0}\cos\psi_a\big|_{t=0} &&= x_{a0} \\ \left.\frac{\partial x_a}{\partial t}\right|_{t=0} &= -x_{a0}\sin\psi_a\tfrac{\psi_t}{2}\Big|_{t=0} &&= 0 \\ \left.\frac{\partial^2 x_a}{\partial t^2}\right|_{t=0} &= -x_{a0}\cos\psi_a\tfrac{\psi_t^2}{4}\Big|_{t=0} &&= -x_{a0}\frac{\psi_t^2}{4} \end{aligned} \tag{2.11}$$

$$\begin{aligned} y_a\big|_{t=0} &= x_{a0}\sin\psi_a\big|_{t=0} &&= 0 \\ \left.\frac{\partial y_a}{\partial t}\right|_{t=0} &= x_{a0}\cos\psi_a\tfrac{\psi_t}{2}\Big|_{t=0} &&= x_{a0}\frac{\psi_t}{2} \\ \left.\frac{\partial^2 y_a}{\partial t^2}\right|_{t=0} &= -x_{a0}\sin\psi_a\tfrac{\psi_t^2}{4}\Big|_{t=0} &&= 0 \end{aligned} \tag{2.12}$$

$$\begin{aligned} z_a\big|_{t=0} &= r_a\sin\theta_a \\ \left.\frac{\partial z_a}{\partial t}\right|_{t=0} &= 0 \\ \left.\frac{\partial^2 z_a}{\partial t^2}\right|_{t=0} &= 0. \end{aligned} \tag{2.13}$$

2.4.2 Linear Flight Path Definition

For the linear flight path, we align the coordinate system such that the sensor flies in the y-dimension. As in the circular case, we have a constant elevation, z_a, but here the x-coordinate, x_a, is also constant. We define the length of the synthetic aperture as L_a, where $-L_a/2 \leq y_a(t) \leq L_a/2$. Since $-1 \leq t \leq 1$ is the defined time interval of the synthetic aperture,

$$y_a(t) = \frac{L_a}{2}t. \tag{2.14}$$

In this dissertation, we assume that the radar is collected broadside with no squinting of the antenna. Thus, the flight path is centered at $y = 0$. As in the circular case, we continue by calculating the first and second derivatives of the flight path:

$$\begin{aligned} x_a\Big|_{t=0} &= x_a \\ \frac{\partial x_a}{\partial t}\Big|_{t=0} &= 0 \\ \frac{\partial^2 x_a}{\partial t^2}\Big|_{t=0} &= 0 \end{aligned} \tag{2.15}$$

$$\begin{aligned} y_a\Big|_{t=0} &= \frac{L_a}{2}t\Big|_{t=0} = 0 \\ \frac{\partial y_a}{\partial t}\Big|_{t=0} &= \frac{L_a}{2}\Big|_{t=0} = \frac{L_a}{2} \\ \frac{\partial^2 y_a}{\partial t^2}\Big|_{t=0} &= 0\Big|_{t=0} = 0 \end{aligned} \tag{2.16}$$

$$\begin{aligned} z_a\Big|_{t=0} &= z_a \\ \frac{\partial z_a}{\partial t}\Big|_{t=0} &= 0 \\ \frac{\partial^2 z_a}{\partial t^2}\Big|_{t=0} &= 0. \end{aligned} \tag{2.17}$$

The above assumes a broadside collection, or zero squint. To consider at non broadside collections, we modify (2.14) to include a constant offset, y_0, such that

$$y_a(t) = \frac{L_a}{2}t + y_0. \tag{2.18}$$

Here, the squint angle, θ_s, is related to y_0 and x_a by a simple relationship,

$$y_0 = x_a \tan\theta_s. \tag{2.19}$$

The only change to (2.15), (2.16), and (2.17) when a squint angle is included is that

$$y_a\Big|_{t=0} = y_0. \tag{2.20}$$

2.5 Description of SAR Datasets

In this section, we describe the simulated and measured datasets used in the experiments performed for this dissertation.

2.5.1 Point Target Scene

Many of the concepts developed in this dissertation are illustrated using a point target simulation in MATLAB. Using the definitions from Section 2.2, we generate a grid of point targets using (2.4) to create the simulated phase history data. In order to illustrate the effects of defocus and distortion caused by PFA, we generate point targets at a very short range from the sensor to accentuate the image artifacts.

We generated a synthetic target scene with a grid of point targets spaced at 5-meter intervals extending from -45 m to 45 m in both x and y directions. Figure 2.2 depicts the locations of the targets in the scene. In this dissertation, we call this dataset the Point Target Scene.

Figure 2.3 shows an image of the Point Target Scene formed using BPA described in Section 2.3.1 with a circular flight path. Because BPA was used to form this image, there are no artifacts in the image due to errors induced by the IFP. All of the targets appear at the correct locations, so there is no distortion in the image.

However, since the simulated scene was set up at very short range, the appearance of the point targets in the image varies significantly across the image. Each target has a sidelobe pattern which looks like a cross that is aligned with range and cross range. This cross pattern is horizontal and vertical at scene center, but it appears to rotate towards the

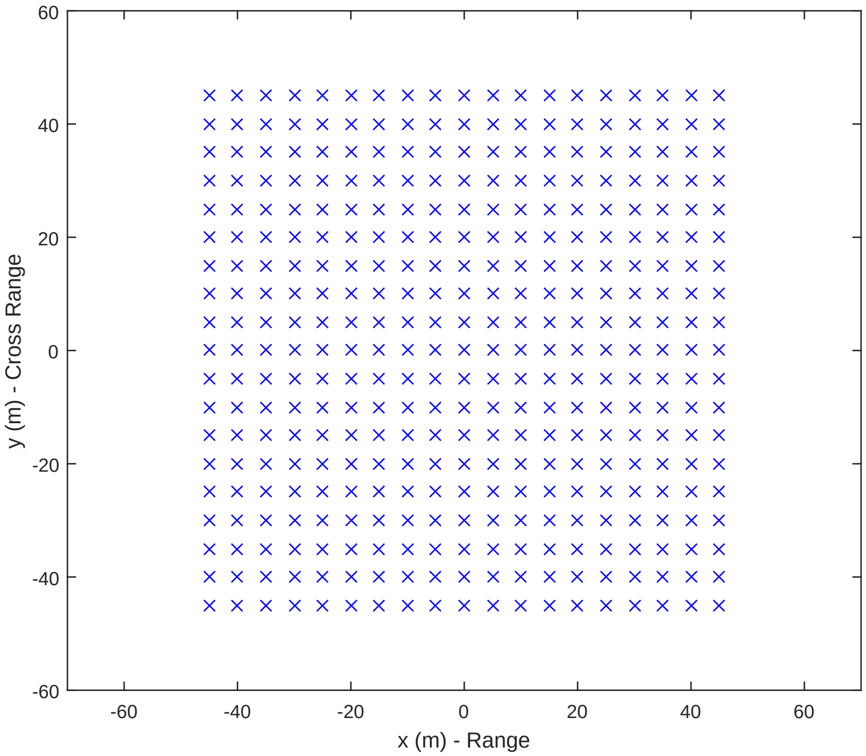

Figure 2.2: Location of synthetic targets in the Point Target Scene

edges of the scene. This is due to range curvature induced by the short range of the sensor.

Also, the size of the point targets appear to change across the image. The size of the target represents the radar resolution at that location. Targets closer to the radar (such as the target at $(x, y) = (45, 0)$ are elongated in the range dimension. This is due to the steeper depression angle that occurs at the shorter ranges.

2.5.2 AFRL Dataset

This dissertation also utilizes a measured dataset provided by the Air Force Research Laboratory (AFRL) [42]. The dataset was collected by a radar platform that was flying a nominally circular flight path. Due to normal aircraft turbulence, an exact circular flight path is not feasible, so a linear least squares fit was performed to determine the best fit to an ideal circular flight path. The best fit is $r_a = 10.4994$ km, $\theta_a = 44.341°$, and $\psi_t = 3.322°$. This ideal circular flight path has a mean squared error of 6.53 m with respect to the actual flight

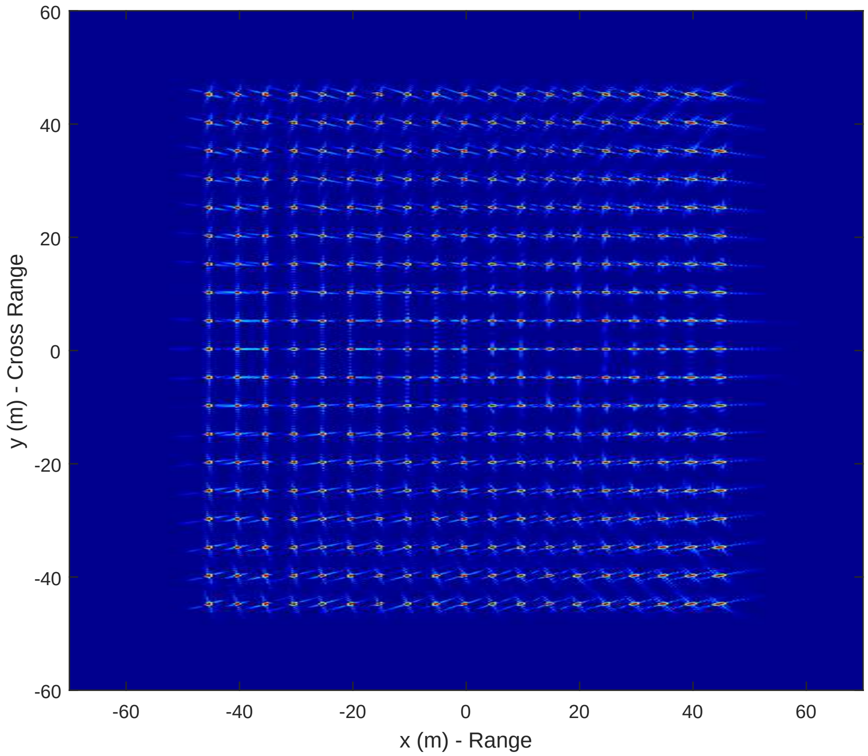

Figure 2.3: BPA image of Point Target Scene - Circular Flight Path

path. The desired image area is a large scene with dimensions of 6 km x 6 km. Despite using a least squares circular fit to the actual flight path, our approach will be shown to be nonetheless effective, and therefore realistically robust to realizable circular flight paths.

The dataset consists of 30,000 pulses with 21,232 complex samples per pulse. Using all of the data results in image resolution of about one foot by one foot.

2.6 Chapter Summary

This chapter included several background items that provide context for the research described in the dissertation. This includes a thorough literature review, a description of the image geometry, and definitions and conventions used for the linear and circular flight paths. It also describes the two IFP algorithms used in the dissertation, namely PFA and BPA. Finally, we briefly described a method for creating a simulated dataset and described one measured dataset that will be used in subsequent chapters.

Chapter 3

Phase Error Analysis and Distortion Correction for PFA

In this chapter, we present a novel method for analyzing phase errors in PFA. Here, we expand upon previous analysis [29] by computing the Taylor Expansion in the data domain as a function of slow time instead of in the image domain. This results in a more accurate analysis as all constant, linear, and quadratic terms are identified. Also, we perform the initial derivation using an arbitrary flight path, and then provide examples using circular and linear flight paths.

In [29], a Taylor Expansion of the differential range was used to calculate the maximum radius of an image without defocus effects for a linear flight path. In that paper, a second-order Taylor Expansion was calculated in the image domain and the terms containing QPE were analyzed to determine the maximum scene size. The result was a specified maximum scene radius, implying a circular region of acceptable focus.

The remainder of this chapter is outlined as follows. Section 3.1 describes the novel approach for analyzing the phase errors that arise from PFA. Section 3.2 describes the Taylor Expansions of the differential range in detail for BPA and PFA. Section 3.3 uses the constant and linear phase error terms derived in Sections 3.1 and 3.2 to accurately describe the distortion in PFA images. Analytic expressions for the distortion effect are derived and illustrated for three types of flight paths: linear, circular, and linear with squint. This analysis is also included in a journal paper [32] which was accepted for publication in 2015. Preliminary results were also published in a 2013 letter [33].

3.1 Phase Error Analysis

Due to the nature of SAR imaging, the phase of the receiver output is more important [12] than the magnitude. Phase errors lead to artifacts in the imagery, such as distortion and defocus. In this section, we analyze the phase response from an ideal point target, which is described in Section 2.2. (2.4) represents the receiver output of an ideal point target, so we define the phase of the ideal point target as

$$\Phi(t) = \frac{-4\pi \Delta R(t)}{\lambda} \tag{3.1}$$

where λ is the center wavelength of the radar pulse.

We wish to decompose $\Phi(t)$ into separate components which are associated with specific effects on the resultant image. For instance, components of $\Phi(t)$ which have a linear relationship with time result in a shift of the target in the image, due to the properties of Fourier transform pairs where a phase ramp shifts a signal in time. Hence, we define

$$\Phi(t) = \Phi_0 + \Phi_1 t + \Phi_2 t^2 + \dots \tag{3.2}$$

In this dissertation, we focus our attention on Φ_0, Φ_1 and Φ_2. The constant and linear terms, Φ_0 and Φ_1, determine the location of the target in the image. If the IFP introduces errors in Φ_0 or Φ_1, targets will not appear in the image at the correct location. This phenomenon is called distortion. The quadratic term, Φ_2, determines the focus of the target in the image. If the IFP introduces errors in Φ_2, targets will appear smeared in cross-range.

This phenomenon is called defocus. Cubic and higher order terms are ignored in this analysis as they do not directly contribute to image distortion or defocus. Cubic phase errors cause the mainlobe to deform and to create asymmetrical sidelobes. Higher order terms tend to impact the sidelobe region instead of the mainlobe [12].

In Section 2.1.2, we described several approaches in the literature to perform this decomposition. Most previous analyses have performed a 2-D Taylor Expansion of Φ in either the image domain or the phase history domain. Here, we will perform a 1-D Taylor Expansion of $\Phi(t)$ in the time dimension. Since the only term in (3.1) that is dependent on time is ΔR, we will perform a second order Taylor Expansion of the differential range, ΔR, which is defined in (2.5). The Taylor Expansion for the differential range is defined [121] as

$$\begin{aligned} \Delta R(t) &\approx \Delta R\big|_{t=0} + \left.\frac{\partial \Delta R}{\partial t}\right|_{t=0} t + \left.\frac{\partial^2 \Delta R}{\partial t^2}\right|_{t=0} \frac{t^2}{2} \qquad (3.3) \\ &\approx \left(r_p\big|_{t=0} - r_a\big|_{t=0} \right) + \left(\left.\frac{\partial r_p}{\partial t}\right|_{t=0} - \left.\frac{\partial r_a}{\partial t}\right|_{t=0} \right) t + \left(\left.\frac{\partial^2 r_p}{\partial t^2}\right|_{t=0} - \left.\frac{\partial^2 r_a}{\partial t^2}\right|_{t=0} \right) \frac{t^2}{2} \end{aligned}$$

with the time dependency of $r_p(t)$ and $r_a(t)$ suppressed for compactness.

Substituting the expansion of ΔR from (3.3) into the expansion of Φ in (3.2) given the phase definition of (3.1) gives the constant, linear, and quadratic components of the point target phase response:

$$\Phi_0 = \frac{-4\pi}{\lambda} \, \Delta R\big|_{t=0} \qquad (3.4)$$

$$\Phi_1 = \frac{-4\pi}{\lambda} \left.\frac{\partial \Delta R}{\partial t}\right|_{t=0} \qquad (3.5)$$

$$\Phi_2 = \frac{-2\pi}{\lambda} \left.\frac{\partial^2 \Delta R}{\partial t^2}\right|_{t=0} . \qquad (3.6)$$

In this dissertation, we define Φ as the exact target phase, $\hat{\Phi}$ as the approximated target phase compensated by PFA, and $\tilde{\Phi}$ as the residual phase error after PFA such that

$$\tilde{\Phi} = \Phi - \hat{\Phi} \tag{3.7}$$

$$\tilde{\Phi} = \tilde{\Phi}_0 + \tilde{\Phi}_1 + \tilde{\Phi}_2 \tag{3.8}$$

where

$$\tilde{\Phi}_0 = \Phi_0 - \hat{\Phi}_0 \tag{3.9}$$

$$\tilde{\Phi}_1 = \Phi_1 - \hat{\Phi}_1 \tag{3.10}$$

$$\tilde{\Phi}_2 = \Phi_2 - \hat{\Phi}_2. \tag{3.11}$$

Correspondingly, we define ΔR as the exact differential range to the target and $\Delta\hat{R}$ as the approximated differential range for PFA, with time dependency suppressed for compactness. From (2.8)

$$\Delta\hat{R} = \frac{-1}{r_a}(x_a\tilde{x} + y_a\tilde{y} + z_a\tilde{z}) \tag{3.12}$$

where $(\tilde{x}, \tilde{y}, \tilde{z})$ are the distorted coordinates where a target at location (x, y, z) appears in the PFA image. This means that $\hat{\Phi}_0$, $\hat{\Phi}_1$, and $\hat{\Phi}_2$ are represented in terms of the distorted coordinates and not the actual coordinates of the target.

We can derive expressions for $(\tilde{x}, \tilde{y}, \tilde{z})$ in terms of the actual coordinates, (x, y, z), by setting $\tilde{\Phi}_0 = 0$ and $\tilde{\Phi}_1 = 0$. These expressions can then be used to resample the PFA images to correct for distortion effects. In this disseration, we will assume that the image plane is flat and corresponds to the ground plane, so we assume $\tilde{z} = 0$.

These distortion corrections will then be used to solve for $\tilde{\Phi}_2$, which is the residual QPE after PFA, in Chapter 4. It is also important to note that in general, the distortion correction is independent of image resolution and therefore independent of the length of the synthetic aperture.

3.2 Taylor Series Expansions of Differential Range

In this section, we will perform the Taylor Expansion for the differential range, ΔR, with respect to time. The differential range is the distance between the antenna phase center and a target in the scene relative to the distance between the antenna phase center and the center of the scene. Since we assume that the center of the scene is stationary (as in spotlight SAR mode) and that the target location is stationary, the only parameter changing with respect to time is the location of the antenna phase center, (x_a, y_a, z_a). Therefore, the results of the Taylor Expansion will include (x_a, y_a, z_a) and their first two derivatives. In Sections 3.3 and 4.2, we will consider the cases of linear and circular flight paths, where many of the derivatives in the corresponding Taylor Expansion are zero, which simplifies the expressions considerably.

3.2.1 Differential Range Expansion for BPA

In Section 2.3.1, we described BPA in detail. BPA performs an exact calculation of ΔR for every pulse at every pixel location. Therefore, in this section we will perform a Taylor Expansion of ΔR as defined in (3.3).

$$\Delta R(t) \approx \left(r_p\big|_{t=0} - r_a\big|_{t=0} \right) + \left(\frac{\partial r_p}{\partial t}\bigg|_{t=0} - \frac{\partial r_a}{\partial t}\bigg|_{t=0} \right) t + \left(\frac{\partial^2 r_p}{\partial t^2}\bigg|_{t=0} - \frac{\partial^2 r_a}{\partial t^2}\bigg|_{t=0} \right) \frac{t^2}{2}$$

where r_p is defined in (2.6) to be

$$r_p(t) = \sqrt{(x - x_a(t))^2 + (y - y_a(t))^2 + (z - z_a(t))^2} \tag{3.13}$$

and r_a is defined in (2.2) to be

$$r_a(t) = \sqrt{x_a^2(t) + y_a^2(t) + z_a^2(t)}. \tag{3.14}$$

In (3.13) and (3.14), the dependence on t is explictly referenced but we drop those references going forward in this analysis. Next, we calculate the first and second derivatives of r_p and r_a:

$$\frac{\partial r_p}{\partial t} = \frac{-1}{r_p}\left[(x-x_a)\frac{\partial x_a}{\partial t} + (y-y_a)\frac{\partial y_a}{\partial t} + (z-z_a)\frac{\partial z_a}{\partial t}\right] \tag{3.15}$$

$$\begin{aligned}\frac{\partial^2 r_p}{\partial t^2} = \frac{-1}{r_p}\Bigg[&(x-x_a)\frac{\partial^2 x_a}{\partial t^2} - \left(\frac{\partial x_a}{\partial t}\right)^2 + (y-y_a)\frac{\partial^2 y_a}{\partial t^2} \\ &- \left(\frac{\partial y_a}{\partial t}\right)^2 + (z-z_a)\frac{\partial^2 z_a}{\partial t^2} - \left(\frac{\partial z_a}{\partial t}\right)^2 + \left(\frac{\partial r_p}{\partial t}\right)^2\Bigg]\end{aligned} \tag{3.16}$$

and

$$\frac{\partial r_a}{\partial t} = \frac{1}{r_a}\left[x_a\frac{\partial x_a}{\partial t} + y_a\frac{\partial y_a}{\partial t} + z_a\frac{\partial z_a}{\partial t}\right] \tag{3.17}$$

$$\begin{aligned}\frac{\partial^2 r_a}{\partial t^2} = \frac{1}{r_a}\Bigg[&x_a\frac{\partial^2 x_a}{\partial t^2} + \left(\frac{\partial x_a}{\partial t}\right)^2 + y_a\frac{\partial^2 y_a}{\partial t^2} + \left(\frac{\partial y_a}{\partial t}\right)^2 \\ &+ z_a\frac{\partial^2 z_a}{\partial t^2} + \left(\frac{\partial z_a}{\partial t}\right)^2 - \left(\frac{\partial r_a}{\partial t}\right)^2\Bigg].\end{aligned} \tag{3.18}$$

Therefore, the constant, linear, and quadatic components of the target phase for BPA are:

$$\Phi_0 = \frac{-4\pi}{\lambda}\left(r_p\big|_{t=0} - r_a\big|_{t=0}\right) \tag{3.19}$$

$$\Phi_1 = \frac{-4\pi}{\lambda}\left(\frac{\partial r_p}{\partial t}\bigg|_{t=0} - \frac{\partial r_a}{\partial t}\bigg|_{t=0}\right) \tag{3.20}$$

$$\Phi_2 = \frac{-2\pi}{\lambda}\left(\frac{\partial^2 r_p}{\partial t^2}\bigg|_{t=0} - \frac{\partial^2 r_a}{\partial t^2}\bigg|_{t=0}\right) \tag{3.21}$$

where the derivatives of r_a are given in (3.17) and (3.18) and the derivatives of r_p are given in (3.15) and (3.16).

3.2.2 Differential Range Expansion for PFA

PFA uses a 2-D FFT to efficiently apply the matched filter in SAR image formation, once the phase history data has been resampled to an appropriate rectangular raster. In order to use this computationally efficient approach, a far-field assumption is made. Earlier works [29] analyzed PFA by performing a second-order Taylor Expansion [121] with respect to the image coordinates x and y. Their results showed that the PFA matched filter kernal is computed with an approximation of the differential range

$$\Delta\hat{R}(t) = \frac{-1}{r_a(t)}(x_a(t)\tilde{x} + y_a(t)\tilde{y} + z_a(t)\tilde{z}) \tag{3.22}$$

where $(\tilde{x}, \tilde{y}, \tilde{z})$ are the distorted coordinates where a target at location (x, y, z) appears in the image. Note that we will be forming the image in the ground plane, so $\tilde{z} = 0$, but we will keep $\tilde{z}$ as a variable for now to maintain generality.

In the same manner as BPA in Section 3.2.1, we perform a second order Taylor Expansion of $\Delta\hat{R}$ with respect to slow time, t, yielding

$$\Delta\hat{R} = \Delta\hat{R}\Big|_{t=0} + \frac{\partial\Delta\hat{R}}{\partial t}\Bigg|_{t=0} t + \frac{\partial^2\Delta\hat{R}}{\partial t^2}\Bigg|_{t=0}\frac{t^2}{2} \tag{3.23}$$

where

$$\frac{\partial\Delta\hat{R}}{\partial t} = \frac{\tilde{x}}{r_a^2}\left(x_a\frac{\partial r_a}{\partial t} - r_a\frac{\partial x_a}{\partial t}\right) + \frac{\tilde{y}}{r_a^2}\left(y_a\frac{\partial r_a}{\partial t} - r_a\frac{\partial y_a}{\partial t}\right) + \frac{\tilde{z}}{r_a^2}\left(z_a\frac{\partial r_a}{\partial t} - r_a\frac{\partial z_a}{\partial t}\right) \tag{3.24}$$

$$\begin{aligned}\frac{\partial^2\Delta\hat{R}}{\partial t^2} = {} & \frac{\tilde{x}}{r_a^3}\left[r_a x_a\frac{\partial^2 r_a}{\partial t^2} - r_a^2\frac{\partial^2 x_a}{\partial t^2} - 2x_a\left(\frac{\partial r_a}{\partial t}\right)^2 + 2r_a\frac{\partial r_a}{\partial t}\frac{\partial x_a}{\partial t}\right] \\ & + \frac{\tilde{y}}{r_a^3}\left[r_a y_a\frac{\partial^2 r_a}{\partial t^2} - r_a^2\frac{\partial^2 y_a}{\partial t^2} - 2y_a\left(\frac{\partial r_a}{\partial t}\right)^2 + 2r_a\frac{\partial r_a}{\partial t}\frac{\partial y_a}{\partial t}\right] \\ & + \frac{\tilde{z}}{r_a^3}\left[r_a z_a\frac{\partial^2 r_a}{\partial t^2} - r_a^2\frac{\partial^2 z_a}{\partial t^2} - 2z_a\left(\frac{\partial r_a}{\partial t}\right)^2 + 2r_a\frac{\partial r_a}{\partial t}\frac{\partial z_a}{\partial t}\right].\end{aligned} \tag{3.25}$$

Therefore, the constant, linear, and quadatic components of the target phase for PFA are:

$$\hat{\Phi}_0 = \frac{-4\pi}{\lambda} \Delta\hat{R}\Big|_{t=0} \tag{3.26}$$

$$\hat{\Phi}_1 = \frac{-4\pi}{\lambda} \frac{\partial\Delta\hat{R}}{\partial t}\Bigg|_{t=0} \tag{3.27}$$

$$\hat{\Phi}_2 = \frac{-2\pi}{\lambda} \frac{\partial^2\Delta\hat{R}}{\partial t^2}\Bigg|_{t=0} \tag{3.28}$$

where the derivatives of $\Delta\hat{R}$ are given in (3.24) and (3.25).

3.3 Distortion Correction for PFA

Previously, we noted that the target phase terms for PFA in Section 3.2.2 are a function of the apparent target location $(\tilde{x}, \tilde{y}, \tilde{z})$ instead of the actual target location (x, y, z). The difference between the actual location of the target and its apparent location in the PFA image is commonly reffered to as distortion. In order to correct for the distortion in the image, we set $\tilde{\Phi}_0 = 0$ and $\tilde{\Phi}_1 = 0$, where $\tilde{\Phi}_0$ was defined in (3.9) and $\tilde{\Phi}_1$ was defined in (3.10);

$$\tilde{\Phi}_0 = \Phi_0 - \hat{\Phi}_0 = 0 \tag{3.29}$$

$$\tilde{\Phi}_1 = \Phi_1 - \hat{\Phi}_1 = 0 \tag{3.30}$$

which implies that

$$\Phi_0 = \hat{\Phi}_0 \tag{3.31}$$

$$\Phi_1 = \hat{\Phi}_1. \tag{3.32}$$

Therefore, we substitute (3.19) and (3.20) from BPA and (3.26) and (3.27) from PFA into (3.31) and (3.32) yielding the following expressions:

$$r_p\big|_{t=0} - r_a\big|_{t=0} = \Delta\hat{R}\Big|_{t=0} \tag{3.33}$$

$$\left.\frac{\partial r_p}{\partial t}\right|_{t=0} - \left.\frac{\partial r_a}{\partial t}\right|_{t=0} = \left.\frac{\partial \Delta\hat{R}}{\partial t}\right|_{t=0} \tag{3.34}$$

Equations (3.33) and (3.34) provide a concise mapping between the exact target location, (x, y, z), and the apparent target location in the PFA image, $(\tilde{x}, \tilde{y})$. In this form, it is not intuitive that these expressions are useful; therefore, in the next few subsections, we will derive the distortion effects for linear and circular flight paths and illustrate distortion corrections using the Point Target Scene and the AFRL Dataset..

3.3.1 Distortion Correction for a Linear Flight Path

In Section 2.4.2, we defined a parameterization for a linear flight path and calculated the first and second derivatives of the flight path given the antenna phase center at (x_a, y_a, z_a). Substituting (2.15), (2.16), and (2.17) into (3.33) and (3.34) gives:

$$r_{p0} - r_{a0} = -\frac{1}{r_{a0}}\left(x_a\tilde{x} + z_a\tilde{z}\right) \tag{3.35}$$

$$-\frac{1}{r_{p0}}\left(y \cdot \frac{L_a}{2}\right) = \frac{\tilde{y}}{r_{a0}^2}\left(-r_{a0} \cdot \frac{L_a}{2}\right). \tag{3.36}$$

Setting $\tilde{z} = 0$ and solving for $\tilde{x}$ and $\tilde{y}$ gives the following expressions:

$$\tilde{x} = \frac{r_{a0}}{x_a}(r_{a0} - r_{p0}) \tag{3.37}$$

$$\tilde{y} = \frac{r_{a0}}{r_{p0}}y \tag{3.38}$$

where

$$r_{p0} = \sqrt{(x - x_a)^2 + y^2 + (z - z_a)^2} \tag{3.39}$$

$$r_{a0} = \sqrt{x_a^2 + z_a^2}. \tag{3.40}$$

To illustrate the distortion effect caused by PFA, we use the Point Target Scene described in Section 2.5.1. The Point Target Scene was generated using a linear flight path with a constant altitude of $z_a = 75$ m and a constant x-position of $x_a = 75$ m. This yields an elevation angle of $\theta_a = 45°$ at the center of the aperture measured with respect to the scene center, $(x, y, z) = (0, 0, 0)$. Note that the elevation angle of the antenna phase center with respect to the scene center will not be constant along the linear synthetic aperture. The integration angle was chosen to be $\theta_a = 0.15$ radians, which corresponds to a cross-range resolution of 0.1 m at X-band (with wavelength $\lambda = 0.03$ m). Figure 2.2 depicts the Point Target Scene used in this experiment.

Next, we apply (3.37) and (3.38) to every point target in the scene, yielding the apparent location of the targets in the PFA image. Figure 3.1 depicts the locations of the grid of point targets in the distorted grid, indexed by $\tilde{x}$ and $\tilde{y}$.

Figure 3.2 is the resulting SAR image using PFA. Note that the geometry of this *small* scene was chosen to accentuate the defocus and distortion effects, which can easily be seen in this image.

To perform the distortion correction after PFA, we lay out a rectangular grid in the target coordinate space, regularly spaced in x and y. Then, we use (3.37) and (3.38) to calculate the distorted location of every pixel in the grid. Since the PFA image is regularly spaced in $\tilde{x}$ and $\tilde{y}$, a 2-D interpolation to the distorted grid is required to correct the distortion effects of PFA. Figure 3.3 is the resulting SAR image after the distortion correction is applied. Note that the targets now appear in the correct location, although many targets are defocused due to uncompensated QPE. The defocus will be addressed in Chapter 4.

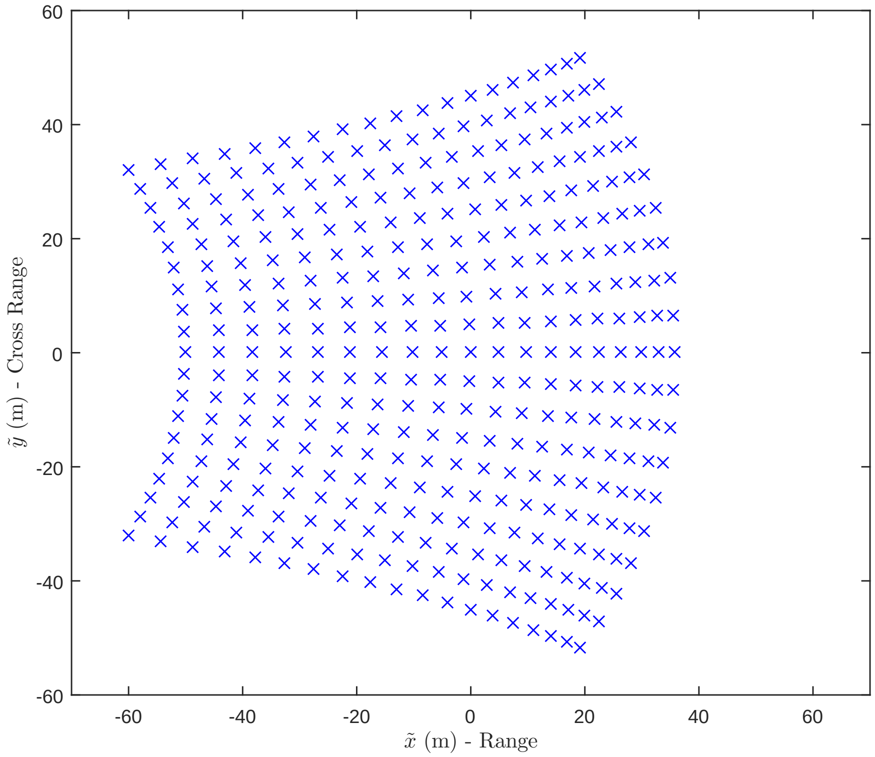

Figure 3.1: Location of synthetic targets in distorted imaging grid - Linear flight path

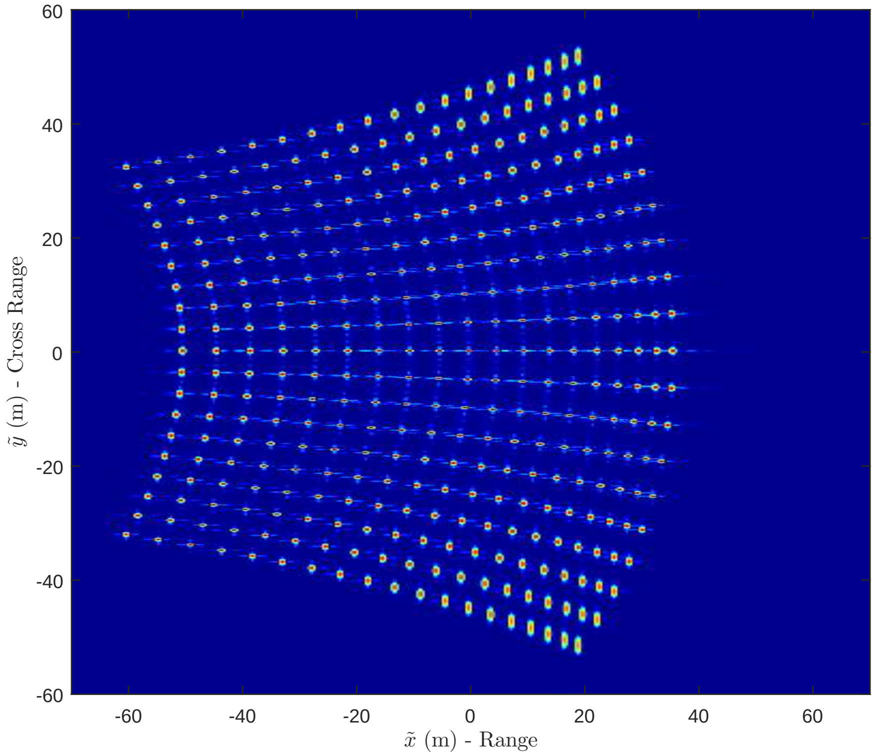

Figure 3.2: PFA image of the Point Target Scene - Linear flight path

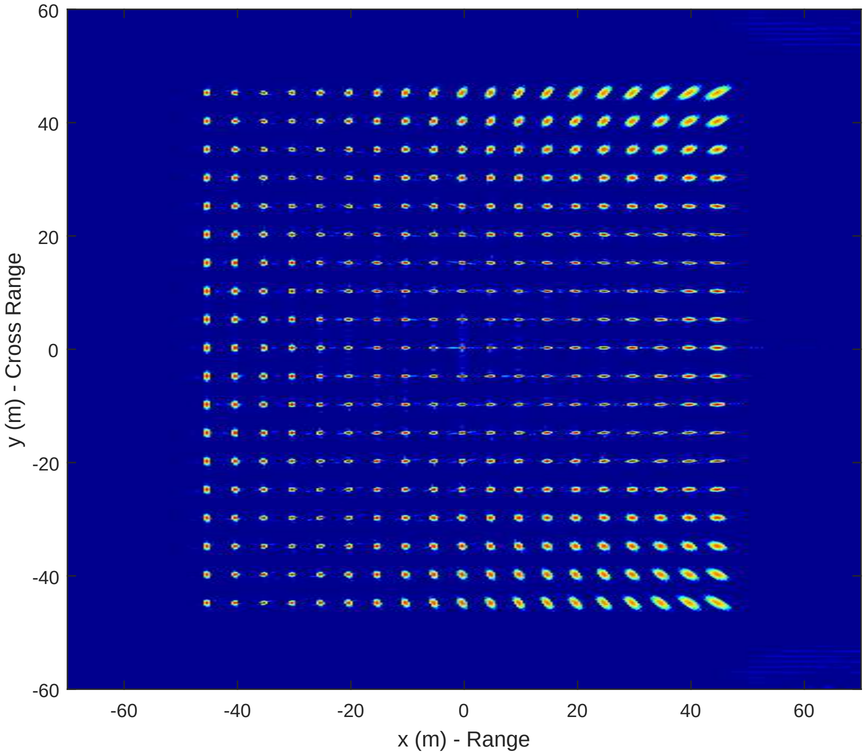

Figure 3.3: PFA image with distortion correction - Linear Flight Path

3.3.2 Distortion Correction for a Circular Flight Path

In Section 2.4.1, we defined a parameterization for a circular flight path and calculated the first and second derivatives of the flight path given the antenna phase center at (x_a, y_a, z_a). Substituting (2.11), (2.12), and (2.13) into (3.33) and (3.34) gives:

$$r_{p0} - r_a = -\frac{1}{r_a}\left(x_{a0}\tilde{x} + r_a \sin\theta_a \tilde{z}\right) \tag{3.41}$$

$$-\frac{1}{r_{p0}}\left(y \cdot x_{a0}\frac{\psi_t}{2}\right) = \frac{\tilde{y}}{r_a^2}\left(-r_a \cdot x_{a0}\frac{\psi_t}{2}\right). \tag{3.42}$$

Setting $\tilde{z} = 0$ and solving for $\tilde{x}$ and $\tilde{y}$ gives the following expressions:

$$\tilde{x} = \frac{r_a - r_{p0}}{\cos\theta_a} \tag{3.43}$$

$$\tilde{y} = \frac{r_a}{r_{p0}} y \tag{3.44}$$

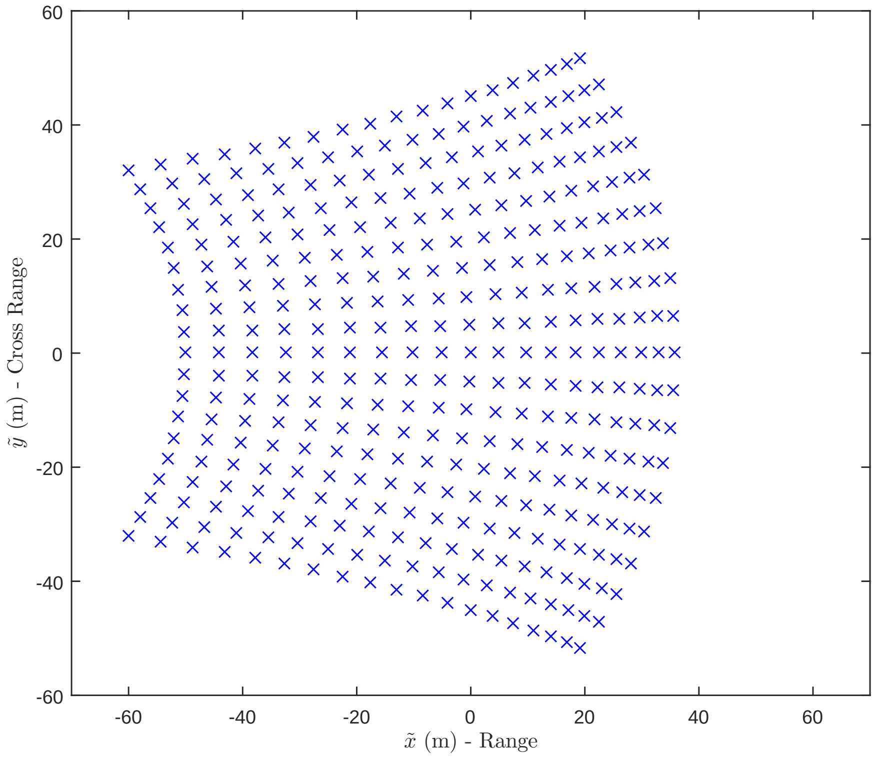

Figure 3.4: Location of synthetic targets in distorted imaging grid - Circular flight path

where

$$r_{p0} = \sqrt{(x - x_{a0})^2 + y^2 + (z - z_a)^2} \tag{3.45}$$

$$x_{a0} = r_a \cos\theta_a. \tag{3.46}$$

To illustrate the distortion effect caused by PFA given a circular flight path, we use the Point Target Scene described in Section 2.5.1. The same synthetic target scene was generated using a circular flight path with a constant altitude of $z_a = 75$ m and a constant elevation angle of $\theta_a = 45°$ measured with respect to the scene center, $(x, y, z) = (0, 0, 0)$. The integration angle was chosen to be $\theta_a = 0.15$ radians, which corresponds to a cross range resolution of 0.1 m at X-band (with wavelength $\lambda = 0.03$m).

Next, we apply (3.43) and (3.44) to every point target in the scene, yielding the apparent location of the targets in the PFA image. Figure 3.4 depicts the locations of a grid of point targets in the distorted grid, indexed by $\tilde{x}$ and $\tilde{y}$.

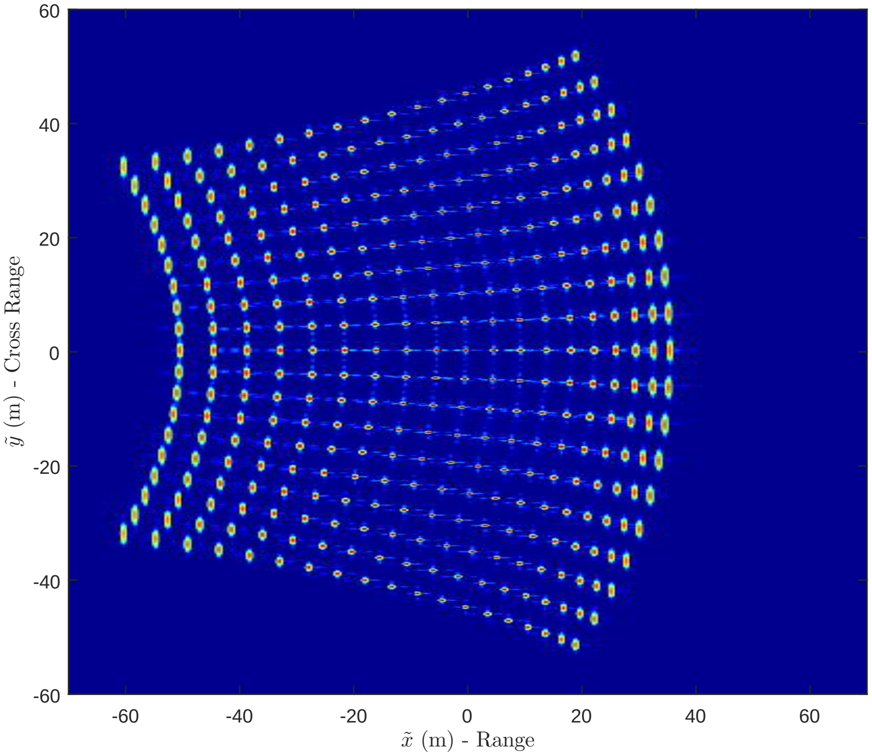

Figure 3.5: PFA image of the Point Target Scene - Circular flight path

Figure 3.5 is the resulting SAR image using PFA. Note again that the geometry of this *small* scene was chosen to accentuate the defocus and distortion effects, which can easily be seen in this image.

Finally, we perform the distortion correction after PFA in the same manner as with the linear flight path. We use (3.43) and (3.44) to calculate the distorted location of every pixel in the grid. Since the PFA image is regularly spaced in $\tilde{x}$ and $\tilde{y}$, a 2-D interpolation to the distorted grid is required to correct the distortion effects of PFA. Figure 3.6 is the resulting SAR image after the distortion correction is applied. Again, the targets now appear in the correct location, although many targets are defocused due to uncompensated QPE. The defocus will be addressed in Chapter 4.

For investigation of circular flight paths, we also use the AFRL Dataset described in Section 2.5.2. Using the best fit of the actual flight path to a circular flight path ($r_a = 10.4994$ km, $\theta_a = 44.341°$, and $\psi_t = 3.322°$), we use (3.43) and (3.44) to calculate the

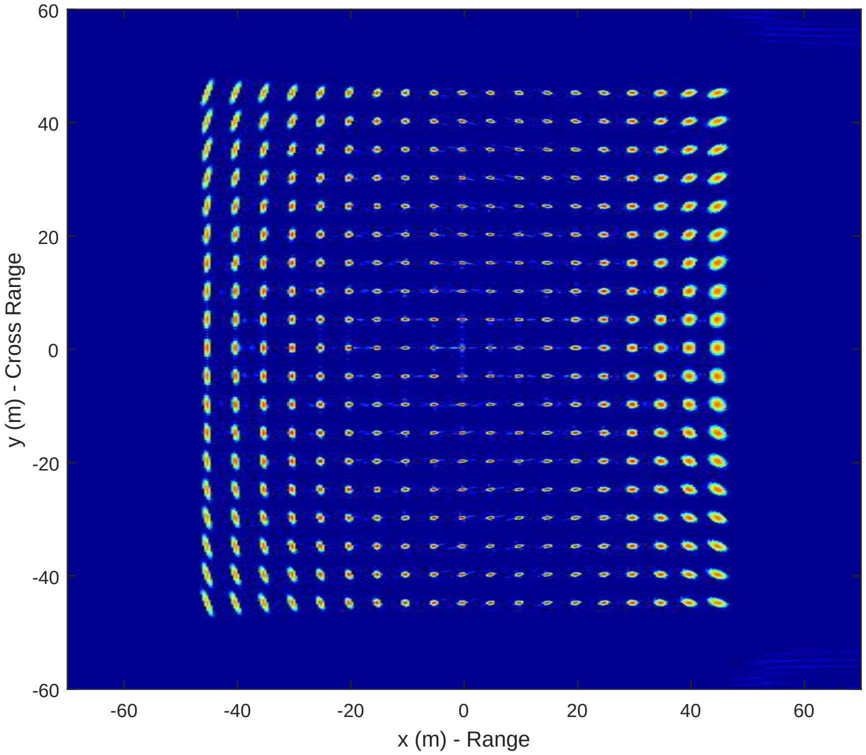

Figure 3.6: PFA image with distortion correction - Circular Flight Path

distortion correction. Figure 3.7 shows the original PFA image while Figure 3.8 shows the same image with the distortion correction applied. Comparing both images, it is clear that the runways and roads in the original image are significantly distorted compared with the corrected image.

3.3.3 Distortion Correction for a Linear Flight Path with Squint

The distortion correction applies equally well to squinted geometries. For a linear flight path with squint, an additional parameter is added to the parameterization of the flight path: y_0. This change is defined in (2.18). Substituting (2.15), (2.16), and (2.17) into (3.33)

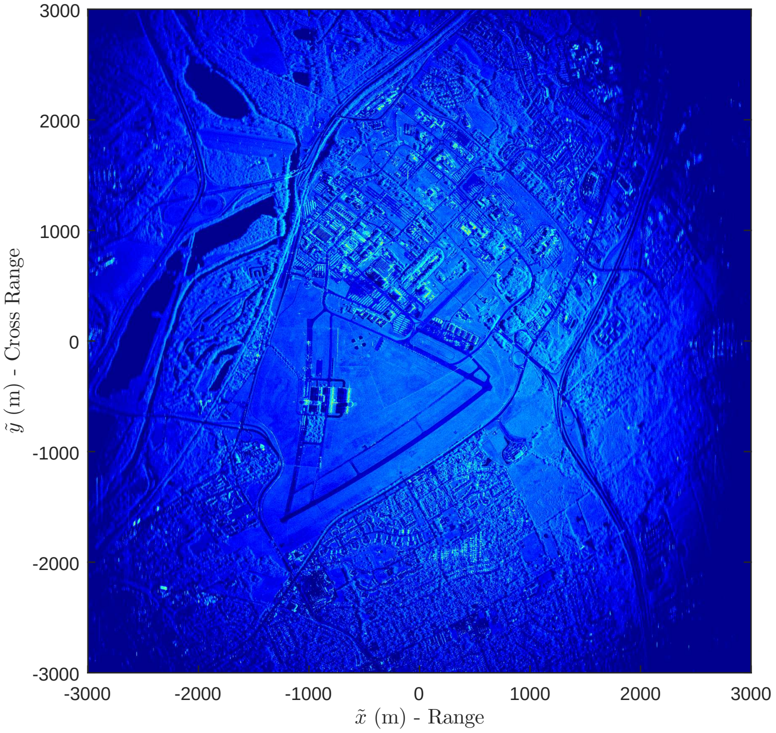

Figure 3.7: PFA image of the AFRL Dataset - Circular Flight Path

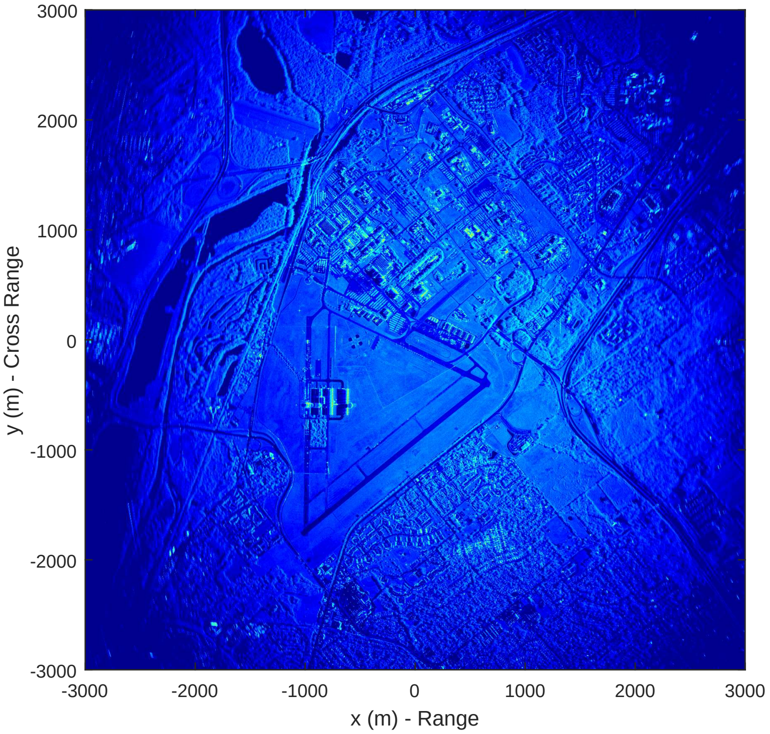

Figure 3.8: PFA image with distortion correction - AFRL Dataset

and (3.34) using the modification in (2.20) gives:

$$r_{p0} - r_{a0} = -\frac{1}{r_{a0}}\left(x_a\tilde{x} + y_0\tilde{y} + z_a\tilde{z}\right) \tag{3.47}$$

$$-\frac{1}{r_{p0}}\left[(y-y_0)\cdot\frac{L_a}{2}\right] - \frac{1}{r_{a0}}\left(y_0\cdot\frac{L_a}{2}\right) = \frac{y_0 L_a}{2r_{a0}^3}\left(x_a\tilde{x} + y_0\tilde{y} + z_a\tilde{z}\right) + \frac{\tilde{y}}{r_{a0}^2}\left(-r_{a0}\cdot\frac{L_a}{2}\right). \tag{3.48}$$

Setting $\tilde{z} = 0$ and solving for $\tilde{x}$ and $\tilde{y}$ gives the following expressions:

$$\tilde{x} = \frac{r_{a0}}{x_a}(r_{a0} - r_{p0}) - \frac{y_0}{x_a}\tilde{y} \tag{3.49}$$

$$\tilde{y} = \frac{r_{a0}}{r_{p0}}y - \frac{y_0}{r_{p0}r_{a0}}(r_{a0} - r_{p0})^2 \tag{3.50}$$

where

$$r_{p0} = \sqrt{(x-x_a)^2 + (y-y_0)^2 + (z-z_a)^2} \tag{3.51}$$

$$r_{a0} = \sqrt{x_a^2 + y_0^2 + z_a^2}. \tag{3.52}$$

As with the linear and circular flight path cases, we illustrate the distortion effect on squinted geometries using the Point Target Scene. The same scene was generated using a linear flight path with a constant altitude of $z_a = 75$ m and a constant x-position of $x_a = 75$ m, but here we add a squint angle of $\theta_s = 45°$, which means the linear offset in the y-dimension is $y_0 = 45$ m.

Next, we apply (3.49) and (3.50) to every point target in the scene, yielding the apparent location of the targets in the PFA image. Figure 3.9 depicts the locations of a grid of point targets in the distorted grid, indexed by $\tilde{x}$ and $\tilde{y}$.

Figure 3.10 is the resulting SAR image using PFA. Note again that the geometry of this *small* scene was chosen to accentuate the defocus and distortion effects, which can easily be seen in this image.

Finally, we perform the distortion correction after PFA in the same manner as the

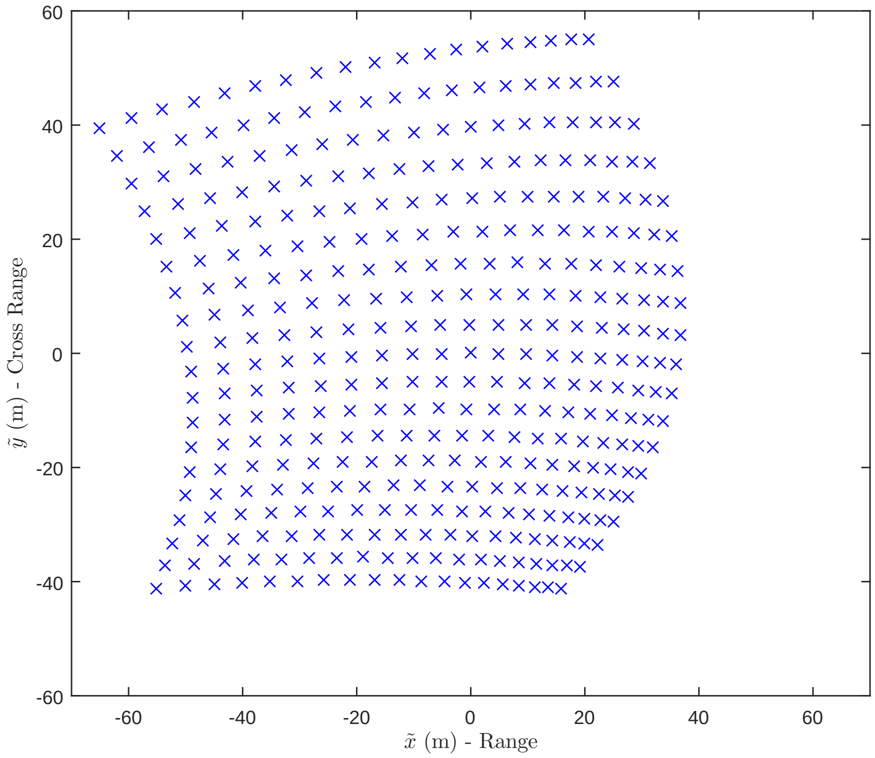

Figure 3.9: Location of synthetic targets in distorted imaging grid - Linear flight path with squint

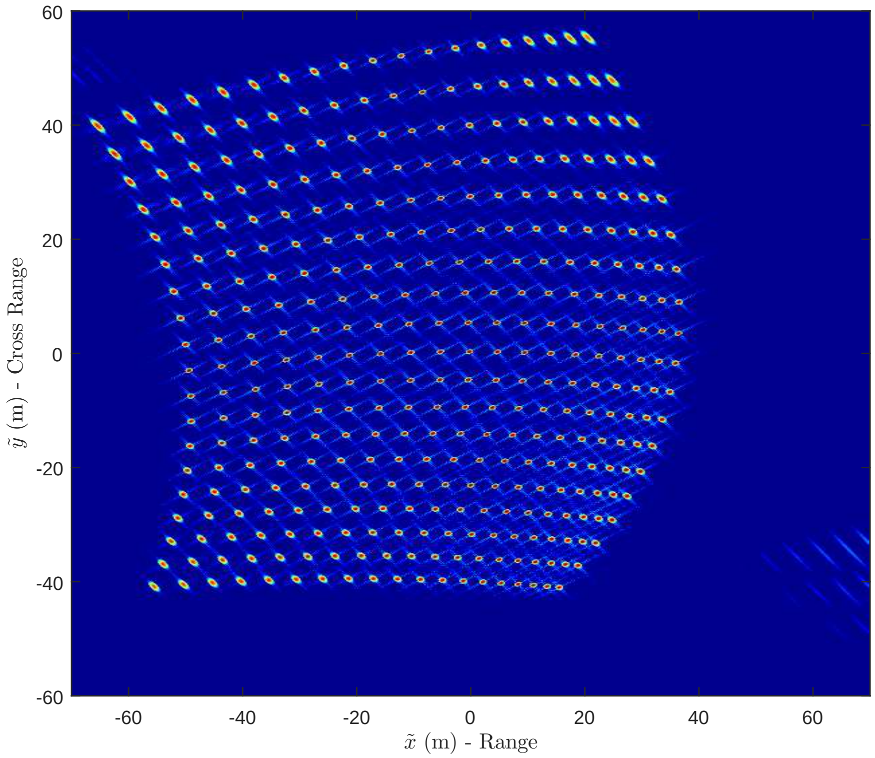

Figure 3.10: PFA image of the Point Target Scene - Linear flight path with squint

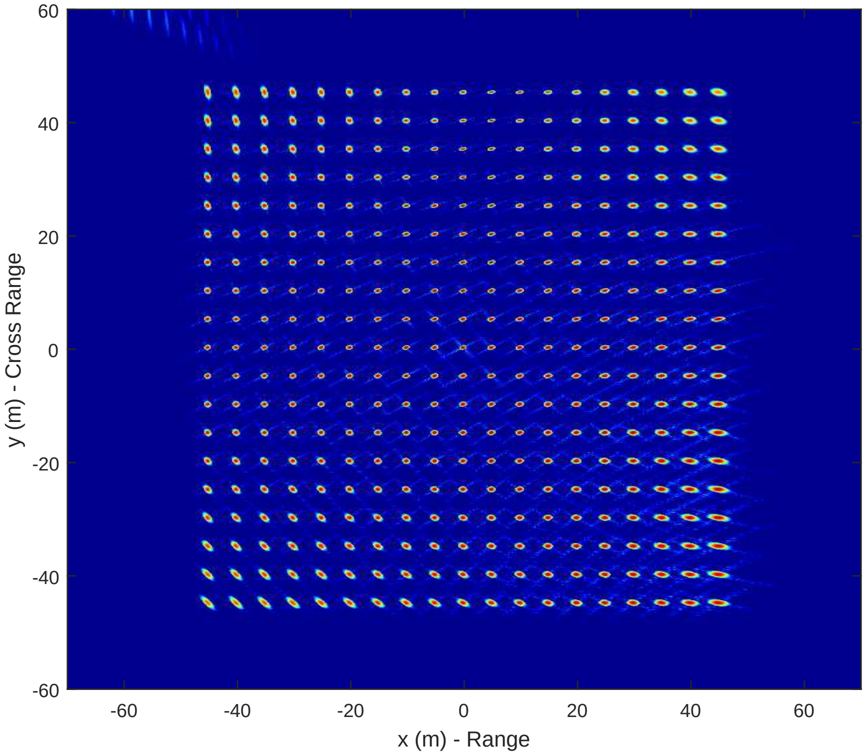

Figure 3.11: PFA image with distortion correction - Linear Flight Path with squint

linear flight path case. We use (3.49) and (3.50) to calculate the distorted location of every pixel in the grid. Since the PFA image is regularly spaced in $\tilde{x}$ and $\tilde{y}$, a 2-D interpolation to the distorted grid is required to correct the distortion effects of PFA. Figure 3.11 is the resulting SAR image after the distortion correction is applied. Again, the targets now appear in the correct location, although many targets are defocused due to uncompensated QPE. The defocus will be addressed in Chapter 4.

3.4 Chapter Summary

In this chapter, we described a novel approach for analyzing phase errors in PFA. We also derived Taylor Expansions of the differential range for both BPA and PFA. Finally, we derived a general distortion correction for PFA and applied it for three types of flight paths: linear, circular, and linear with squint. The QPE derived here will be analyzed in detail in the next section of the dissertation, Chapter 4.

Chapter 4

QPE Analysis and Scene Size Limitations for PFA

In this chapter, we present a novel method for analyzing QPE in PFA. In Chapter 3, we presented a novel method for decomposing the constant, linear, and quadratic phase error terms in PFA. We also showed how the constant and linear terms can be used to derive analytic expressions for the distortion in a PFA image. Here, we build upon that analysis by utilizing the quadratic phase terms to derive analytic expressions for the defocus in PFA.

The important distinction between this analysis and previous results from the literature is that we take into account the distortion as part of the defocus analysis. The quadratic phase terms for BPA are in target coordinates (x, y, z) while the quadratic phase terms for PFA are in the distorted image coordinates $(\tilde{x}, \tilde{y})$. By substituting expressions for $(\tilde{x}, \tilde{y})$ in terms of (x, y, z), accurate analytical expressions are derived for the residual QPE after PFA. This is a substantial departure from earlier analyses that neglected the impact of distortion when determining the region of acceptable focus.

These analytical expressions are then used to determine accurate scene size limitations for PFA. By analyzing contours of acceptable QPE (e.g. $\pi/2$ or $\pi/4$), the allowable scene size is easily determined, and results are notably different from earlier publications which typically described circular regions of acceptable focus. In this dissertation, we determine regions of focus that are arbitrary in shape to account for all areas in the image with acceptable image focus.

The remainder of this chapter is outlined as follows. Section 4.1 continues the phase error analysis from Chapter 3 by analyzing the quadratic components of the image phase. Section 4.2 describes the allowable QPE for a well focused image and derives scene size limitations for circular and linear flight paths. The QPE and scene size limitations are illustrated using the Point Target Scene from Section 2.5.1 and with the large scene AFRL Dataset. Finally, Section 4.3 provides a comparison between the results of this dissertation with previously published analyses. Most of the material from this chapter was originally published in [32] which was accepted for publication in 2015.

4.1 Residual QPE for PFA

In Section 3.1, we described our decomposition of image phase into constant, linear, and quadratic components. In Section 3.3, the constant and linear phase error terms, $\tilde{\Phi}_0$ and $\tilde{\Phi}_1$ respectively, were analyzed, resulting in analytical expressions for PFA image distortion. Here, we concentrate on the quadratic phase terms. The residual QPE, denoted by $\tilde{\Phi}_2$, was defined in (3.11) and repeated here,

$$\tilde{\Phi}_2 = \Phi_2 - \hat{\Phi}_2 \tag{4.1}$$

where Φ_2 is defined in (3.21) and $\hat{\Phi}_2$ is defined in (3.28). The expressions for Φ_2 and $\hat{\Phi}_2$ are repeated here for convenience:

$$\Phi_2 = \frac{-2\pi}{\lambda}\left(\left.\frac{\partial^2 r_p}{\partial t^2}\right|_{t=0} - \left.\frac{\partial^2 r_a}{\partial t^2}\right|_{t=0} \right) \tag{4.2}$$

$$\hat{\Phi}_2 = \frac{-2\pi}{\lambda} \left.\frac{\partial^2 \Delta\hat{R}}{\partial t^2}\right|_{t=0} \tag{4.3}$$

Note these expressions are dependent on the second derivative with respect to time of the differential range for BPA and PFA. The second derivative of the range from the antenna to the target, r_p, is given in (3.16), and the second derivative of the range from the antenna to scene center, r_a, is given in (3.18). Finally, the second derivative of the approximated differential range by PFA, $\Delta\hat{R}$, is given in (3.25).

Remember that $\Delta\hat{R}$ is given in terms of $(\tilde{x}, \tilde{y})$, so we will apply the distortion corrections from Chapter 3 given in (3.33) and (3.34).

In general, the QPE expressions are complicated, but they simplify nicely for some classes of ideal flight paths. In Section 4.2, we examine the QPE for a circular flight path and a linear flight path.

4.2 Scene Size Limitations for PFA

Residual QPE in a SAR image appears as smearing in the cross range dimension, and it significantly affects image interpretation. The total (or center-to-edge) quadratic phase is computed as the difference between the quadratic phase at the center of the aperture ($t = 0$) and one edge of the aperture ($t = 1$). Since we defined the synthetic aperture to occur in the time interval $t \in [-1, 1]$ in Section 2.2, the quadratic phase is simply the Φ_2 term in our decomposition.

Therefore, we will assume that the image is well focused if the quadratic phase compensated in PFA is within $\pi/2$ of $\tilde{\Phi}_2$ [29, 34], although some sources indicate a more stringent requirement of $\pi/4$ [111]. A target at location (x, y, z) will be well focused if the residual QPE, $\tilde{\Phi}_2$, is less than $\pi/2$,

$$\left|\tilde{\Phi}_2\right| < \frac{\pi}{2}. \tag{4.4}$$

The expression in (4.4) is the general form for acceptable image focus. Again, note that the $\Delta\hat{R}$ term is given in distorted image coordinates, so application of the distortion correction is necessary to derive an accurate scene size limitation.

In Sections 4.2.1 and 4.2.2, we look at the two special cases of circular and linear flight paths.

4.2.1 QPE and Scene Size Limitations for a Circular Flight Path

Here we take the derivatives of (x_a, y_a, z_a) calculated in Section 2.4.1 and use the QPE expressions derived in Chapter 3 to find the residual QPE after PFA. First, we substitute (2.11), (2.12), and (2.13) into the second derivatives found in (3.16) and (3.18):

$$\left.\frac{\partial^2 r_p}{\partial t^2}\right|_{t=0} = \frac{x_{a0}\psi_t^2}{4r_{p0}}\left(x - \frac{y^2 x_{a0}}{r_{p0}^2}\right) \tag{4.5}$$

$$\left.\frac{\partial^2 r_a}{\partial t^2}\right|_{t=0} = 0 \tag{4.6}$$

where

$$r_{p0} = \sqrt{(x - x_{a0})^2 + y^2 + (z - z_a)^2}. \tag{4.7}$$

The expression r_{p0} represents the distance between a target at (x, y, z) and the center of the antenna aperture at $t = 0$.

Next we substitute (4.5) and (4.6) into (4.2) to derive Φ_2:

$$\Phi_2 = \frac{-\psi_t^2 \pi x_{a0}}{2\lambda r_{p0}}\left(x - \frac{y^2 x_{a0}}{r_{p0}^2}\right)$$

$$\Phi_2 = A\left(\frac{x}{r_{p0}} - \frac{y^2 x_{a0}}{r_{p0}^3}\right) \tag{4.8}$$

where A is dependent only on the parameters of the circular flight path and the wavelength of the signal; thus, A is constant with respect to target position,

$$A = \frac{-\psi_t^2 \pi x_{a0}}{2\lambda}. \tag{4.9}$$

The expression in (4.8) represents the total amount of quadratic phase in BPA. Now, we substitute the circular flight path expressions from (2.11), (2.12), and (2.13) into (3.25) to determine quadratic components of the differential range for PFA. For the circular case, this simplifies to:

$$\left.\frac{\partial^2 \Delta \hat{R}}{\partial t^2}\right|_{t=0} = \tilde{x} \cos\theta_a \frac{\psi_t^2}{4}. \tag{4.10}$$

Substituting (4.10) into (4.3) gives

$$\begin{aligned}\hat{\Phi}_2 &= \frac{-\pi}{\lambda} \tilde{x} \cos\theta_a \frac{\psi_t^2}{2} \\ \hat{\Phi}_2 &= A\frac{\tilde{x}}{r_a}. \end{aligned} \tag{4.11}$$

Here (4.11) is given as a function of the distorted coordinate, $\tilde{x}$. We want to express $\hat{\Phi}_2$ as a function of the actual target coordinates, so we apply the distortion correction by substituting (3.43) into (4.11) which yields

$$\hat{\Phi}_2 = A\frac{r_a - r_{p0}}{x_{a0}}. \tag{4.12}$$

Therefore, by substituting (4.8) and (4.12) into (4.1), the residual QPE from the PFA is given as

$$\tilde{\Phi}_2 = A\left(\frac{x}{r_{p0}} - \frac{y^2 x_{a0}}{r_{p0}^3} - \frac{\tilde{x}}{r_a}\right). \tag{4.13}$$

$$\tilde{\Phi}_2 = A\left(\frac{x}{r_{p0}} - \frac{y^2 x_{a0}}{r_{p0}^3} + \frac{r_{p0} - r_a}{x_{a0}}\right). \tag{4.14}$$

Substituting (4.14) into (4.4) gives the criteria for a well focused target given a circular flight path,

$$\left|A\left(\frac{x}{r_{p0}} - \frac{y^2 x_{a0}}{r_{p0}^3} + \frac{r_{p0} - r_a}{x_{a0}}\right)\right| < \frac{\pi}{2}. \tag{4.15}$$

A target at scene center is perfectly focused since $\tilde{\Phi}_2 = 0$ at scene center. There also exists a region around the scene center where targets are well focused, denoted by the set of (x, y, z) locations where (4.15) is satisfied, a significant departure from earlier predictions based on spatial analysis that omitted the effects of distortion.

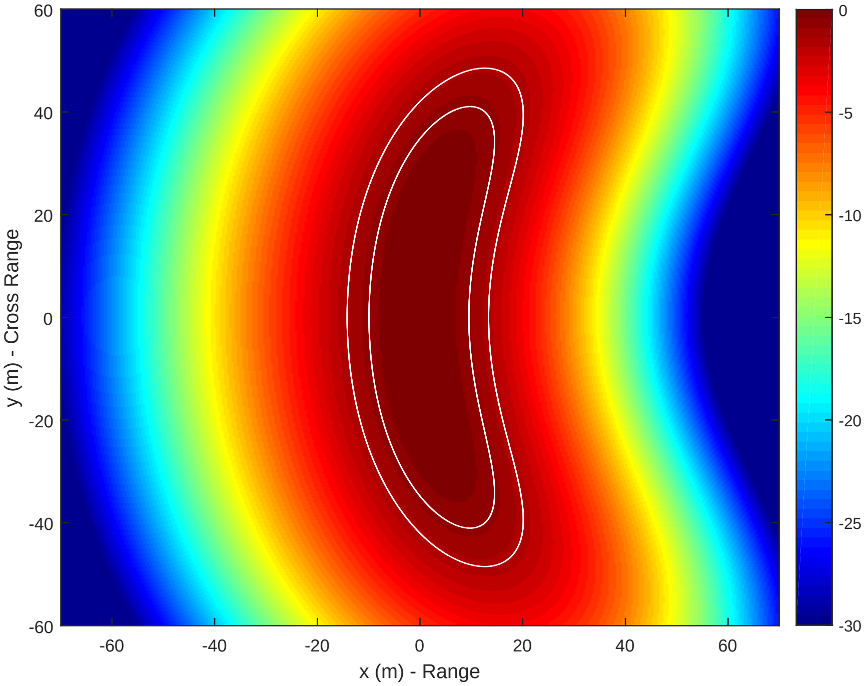

Figure 4.1: Residual QPE after PFA - Circular flight path

Point Target Scene - Circular Flight Path

To illustrate the effects of defocus, we continue with the Point Target Scene first developed in Section 2.5.1. Figure 2.2 depicts the locations of a grid of point targets which appear distorted and defocused in the PFA image in Figure 3.5. After applying the distortion correction, the targets appear in the correct location in Figure 3.6; however, targets near the edges of the scene show significant defocus.

Next, we use (4.14) to plot the residual QPE in terms of the actual target coordinates; this is displayed in Figure 4.1. The region of focus is denoted by the contour lines near the center of the image, where the residual phase error is minimal. The inner contour line denotes an error of $\pi/4$ while the outer contour line denotes an error of $\pi/2$.

Figure 4.2 shows the same PFA image as in Figure 3.5 with the distortion correction applied; here the contour lines of focus are displayed as well. These contour lines are consistent with the pattern of degraded point responses in the image and are notably different from the circular regions of focus determined in earlier works.

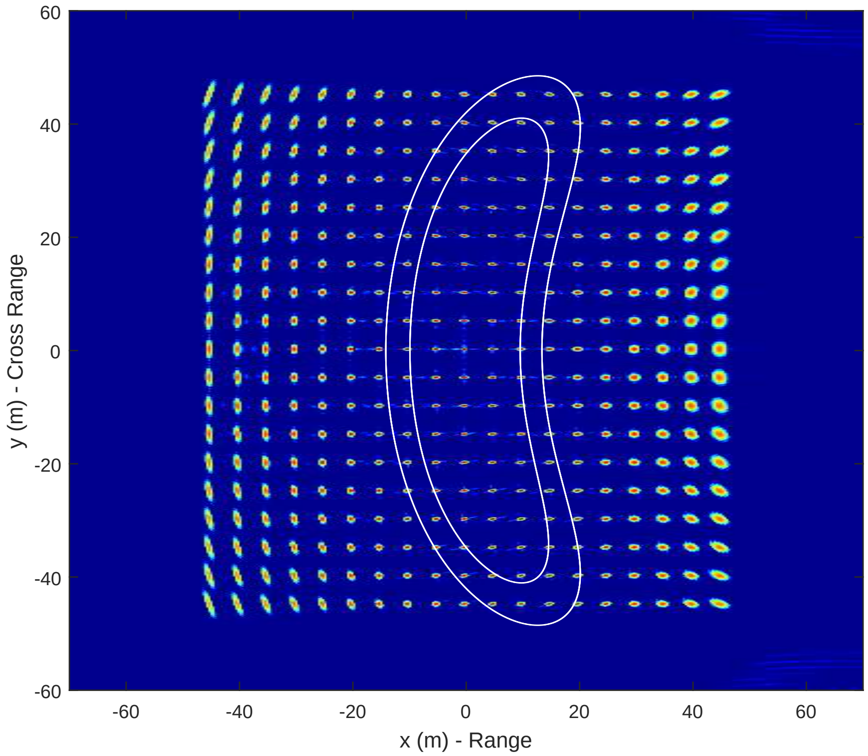

Figure 4.2: PFA image with distortion correction - Circular flight path

AFRL Dataset

We can illustrate the defocus effect better using the large scene AFRL Dataset described in Section 2.5.2. Using the parameters for the flight path given in Section 2.5.2, the residual QPE was calculated using (4.14) and the result is displayed in Figure 4.3. As expected, the center of the image has a residual QPE of 0, which represents perfect focus. Two contour lines are shown, the inner line corresponding to a maximum QPE of $\pi/4$ and the outer line corresponding to a maximum error of $\pi/2$. In this scenario, only 7.8% of the desired image area is within the $\pi/4$ contour and only 11.5% of the desired image area is within the $\pi/2$ contour. This means that most of the image is unacceptably defocused and distorted.

We also include the QPE plot in the distorted PFA image coordinates in Figure 4.4. This shows the residual QPE before the distortion correction is applied. The result shown in distorted coordinates demonstrates that the residual QPE is mostly a function of $\tilde{x}$ (the distorted range coordinate), and that an efficient algorithm can correct the defocus for a

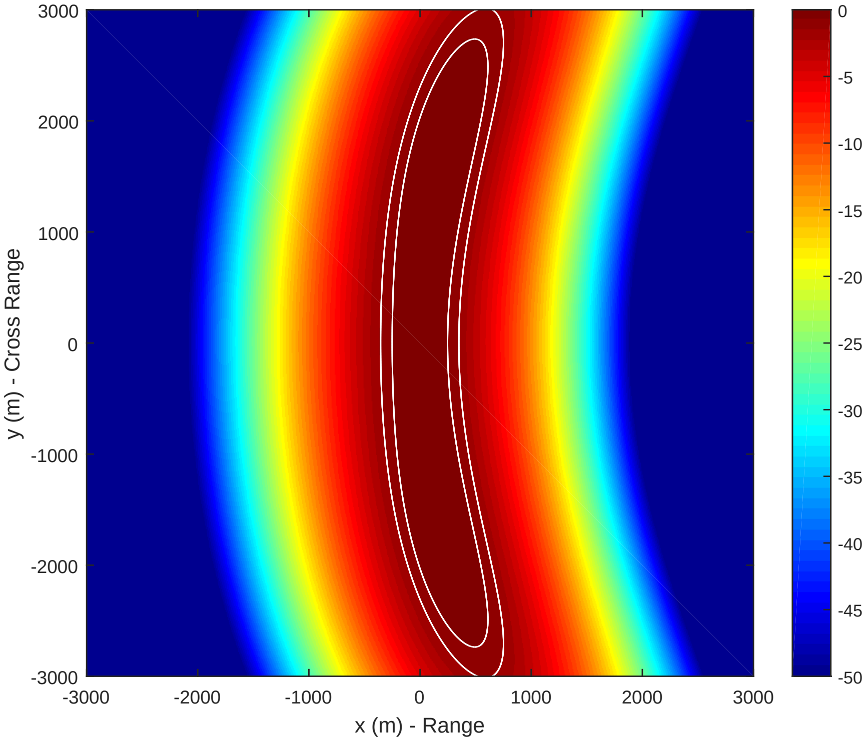

Figure 4.3: Residual QPE after PFA - AFRL Dataset

significant portion of the image. This novel defocus correction algorithm is described in Chapter 5.

4.2.2 QPE and Scene Size Limitations for a Linear Flight Path

As in the circular case, we use the derivatives of the flight path calculated in Section 2.4.2 to find the residual QPE after PFA for the linear case. First we take the derivatives of (x_a, y_a, z_a) found in (2.15), (2.16), and (2.17) and substitute them into the second derivatives found in (3.16) and (3.18):

$$\left.\frac{\partial^2 r_p}{\partial t^2}\right|_{t=0} = \frac{L_a^2}{4}\left(\frac{1}{r_{p0}} - \frac{y^2}{r_{p0}^3}\right) \tag{4.16}$$

$$\left.\frac{\partial^2 r_a}{\partial t^2}\right|_{t=0} = \frac{L_a^2}{4}\frac{1}{r_{a0}} \tag{4.17}$$

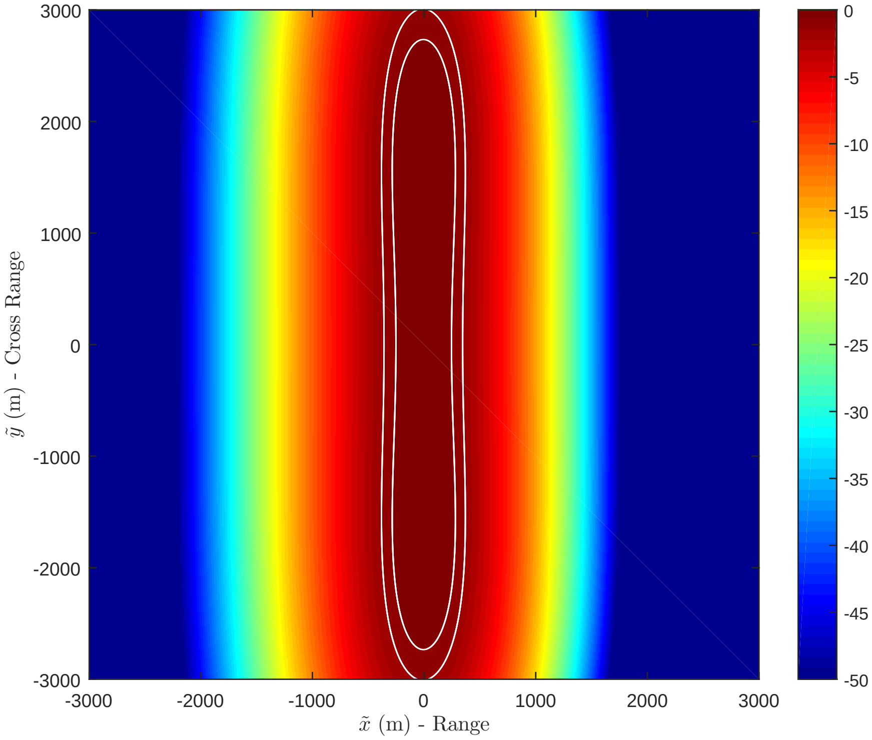

Figure 4.4: Residual QPE after PFA in distorted coordinates - AFRL Dataset

where

$$r_{p0} = \sqrt{(x - x_a)^2 + y^2 + (z - z_a)^2} \tag{4.18}$$

$$r_{a0} = \sqrt{x_a^2 + z_a^2}. \tag{4.19}$$

As in the circular case, the expression r_{p0} represents the distance between a target at (x, y, z) and the center of the antenna aperture at $t = 0$. Here we also calculate r_{a0}, which represents the distance between the center of the scene and the center of the antenna aperture at $t = 0$; note that r_a is not constant throughout the imaging aperture, unlike the circular flight path.

Next we substitute (4.18) and (4.19) into (4.2) to derive Φ_2:

$$\begin{aligned}\Phi_2 &= \frac{-L_a^2\pi}{2\lambda}\left(\frac{1}{r_{p0}} - \frac{1}{r_{a0}} - \frac{y^2}{r_{p0}^3}\right)\\ \Phi_2 &= A\left(\frac{1}{r_{p0}} - \frac{1}{r_{a0}} - \frac{y^2}{r_{p0}^3}\right) \qquad (4.20)\end{aligned}$$

where A is again a constant with respect to target position,

$$A = \frac{-L_a^2\pi}{2\lambda}. \qquad (4.21)$$

The expression in (4.20) represents the total amount of quadratic phase in BPA. Now, we substitute the linear flight path expressions from (2.15), (2.16), and (2.17) into (3.25) to determine quadratic components of the differential range for PFA. For the linear case, this simplifies to

$$\left.\frac{\partial^2 \Delta\hat{R}}{\partial t^2}\right|_{t=0} = \frac{L_a^2}{4r_{a0}^3}(x_a\tilde{x} + z_a\tilde{z}). \qquad (4.22)$$

Substituting (4.22) into (4.3) and setting $\tilde{z} = 0$ gives

$$\begin{aligned}\hat{\Phi}_2 &= \frac{-\pi}{\lambda}\frac{L_a^2}{2r_{a0}^3}x_a\tilde{x}\\ \hat{\Phi}_2 &= A\frac{x_a}{r_{a0}^3}\tilde{x}. \qquad (4.23)\end{aligned}$$

Again (4.23) is given as a function of the distorted coordinate, $\tilde{x}$. We want to express $\hat{\Phi}_2$ as a function of the actual target coordinates, so we apply the distortion correction by substituting (3.37) into (4.11) which yields

$$\begin{aligned}\hat{\Phi}_2 &= A\frac{1}{r_{a0}^2}(r_{a0} - r_{p0})\\ \hat{\Phi}_2 &= A\left(\frac{1}{r_{a0}} - \frac{r_{p0}}{r_{a0}^2}\right). \qquad (4.24)\end{aligned}$$

Substituting (4.20) and (4.24) into (4.1), the residual QPE from the PFA is given as

$$\tilde{\Phi}_2 = A\left(\frac{1}{r_{p0}} - \frac{2}{r_{a0}} - \frac{y^2}{r_{p0}^3} + \frac{r_{p0}}{r_{a0}^2}\right). \tag{4.25}$$

Substituting (4.25) into (4.4) gives the criteria for a well focused target given a linear flight path,

$$\left|A\left(\frac{1}{r_{p0}} - \frac{2}{r_{a0}} - \frac{y^2}{r_{p0}^3} + \frac{r_{p0}}{r_{a0}^2}\right)\right| < \frac{\pi}{2}. \tag{4.26}$$

As with the circular flight path case, a target at scene center is perfectly focused since $\tilde{\Phi}_2 = 0$ at scene center. There also exists a region around the scene center where targets are well focused, denoted by the set of (x, y, z) locations where (4.26) is satisfied; this represents a significant departure from earlier predictions based on spatial analysis that omitted the effects of distortion.

Point Target Scene - Linear Flight Path

As with the circular case, we continue with the Point Target Scene first developed in Section 2.5.1. Figure 2.2 depicts the locations of a grid of point targets which appear distorted and defocused in the PFA image in Figure 3.2. After applying the distortion correction, the targets appear in the correct location in Figure 3.3; however, targets near the edges of the scene show significant defocus.

Next, we use (4.25) to plot the residual QPE in terms of the actual target coordinates. This is displayed in Figure 4.5. The region of focus is denoted by the contour lines near the center of the image, where the residual phase error is minimal. The inner contour line denotes an error of $\pi/4$ while the outer contour line denotes an error of $\pi/2$.

Figure 4.6 shows the same PFA image as in Figure 3.2 with the distortion correction applied; here the contour lines of focus are displayed as well. These contour lines are consistent with the pattern of degraded point responses in the image and are notably different from the circular regions of focus determined in earlier works.

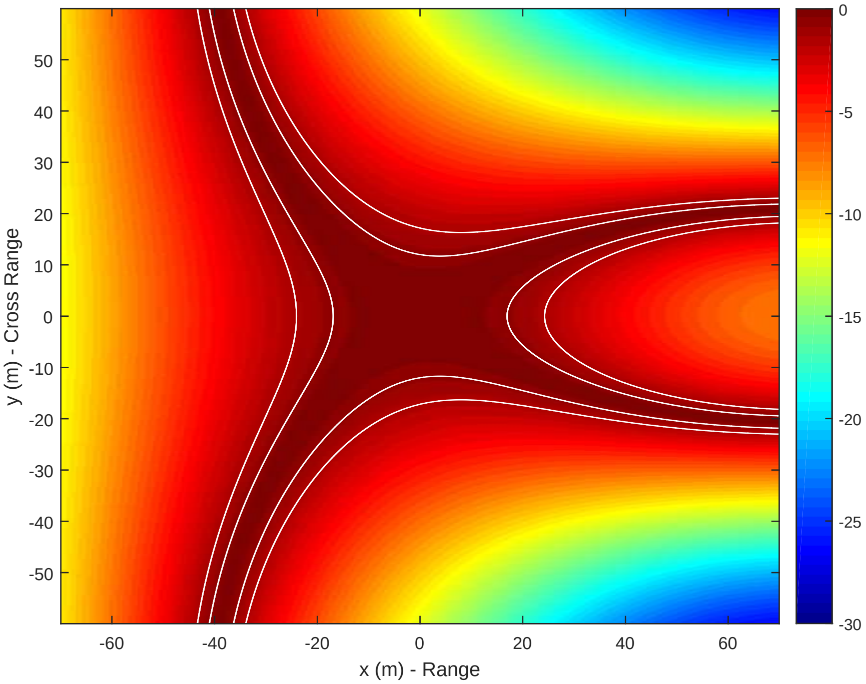

Figure 4.5: Residual QPE after PFA - Linear flight path

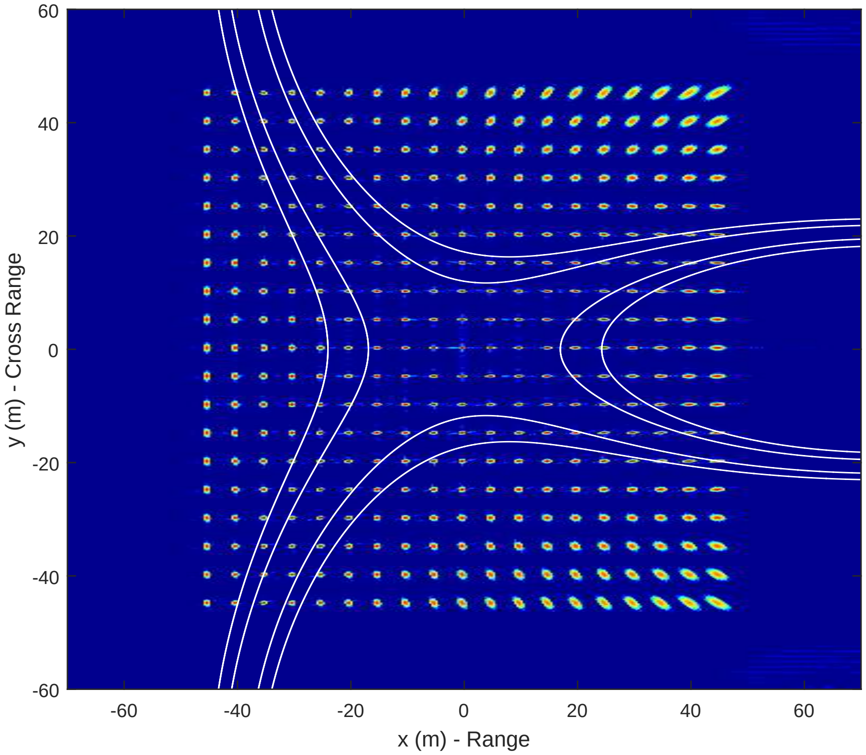

Figure 4.6: PFA image with distortion correction - Linear flight path

4.3 Comparison with Past Published Results

There are several references in the literature that describe scene size limitations for PFA given a linear flight path. In [12], the allowable scene radius, r_{max}, is quantified as

$$r_{max} = 2\rho_a\sqrt{\frac{r_a}{\lambda}} \tag{4.27}$$

where ρ_a is the cross range resolution, which is defined as

$$\rho_a = \frac{r_{a0}\lambda}{2L_a} \tag{4.28}$$

for the special case of broadside imaging with a linear flight path. The authors of [29] and [34] derive a similar expression. These references all cite $\pi/2$ as allowable QPE. In [1], the authors use a tighter phase error requirement of $\pi/4$, and their scene size limit is

$$r_{max} = \rho_a\sqrt{\frac{2r_a}{\lambda}} \tag{4.29}$$

which is consistent with the other results if $\pi/4$ is assumed to be the allowable QPE.

Figure 4.7 shows (4.27) and (4.29) plotted along with the scene size limits derived in this dissertation given a circular flight path. Figure 4.8 shows the same comparison for the linear flight path. Here, (4.27) (derived from a $\pi/2$ QPE limit) is the outer dotted line while (4.29) (derived from a $\pi/4$ QPE limit) is the inner dotted line. Note that these estimates are extremely conservative compared with the limits derived in this paper. For instance, the point target at $(x, y) = (10, 40)$ in the circular case (Figure 4.7) is very well focused and is included in the allowable region from this dissertation, but it is well outside the allowable region from (4.27) and (4.29). In the linear case (Figure 4.8), the point target at $(x, y) = (-40, 45)$ is also very well focused.

Therefore, in this dissertation, we determine regions of focus that are arbitrary in shape to account for all areas in the image with acceptable image focus.

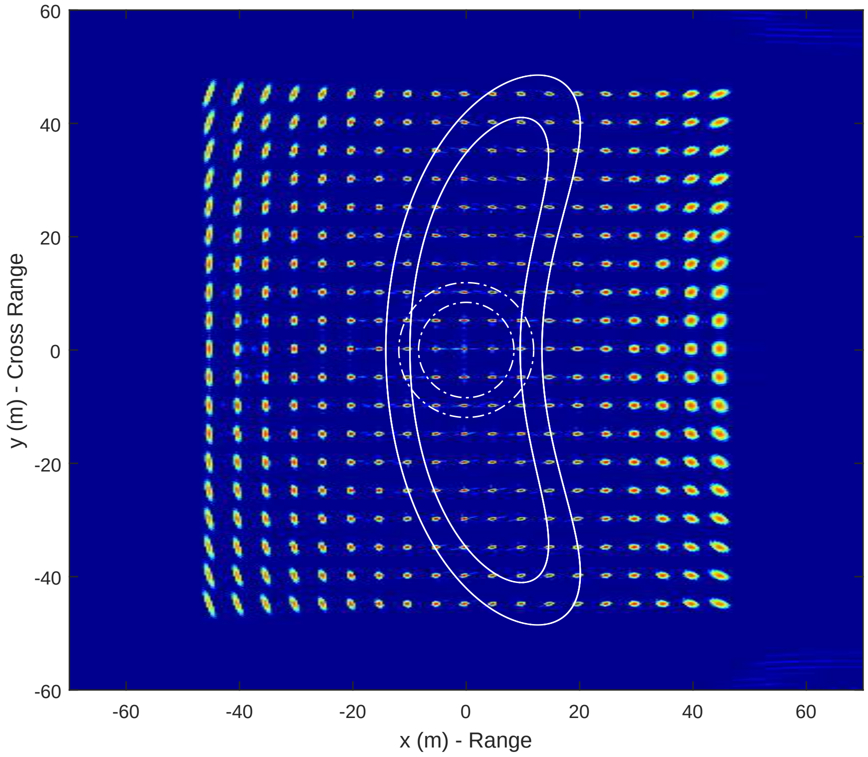

Figure 4.7: Comparison with previously published results - Circular flight path

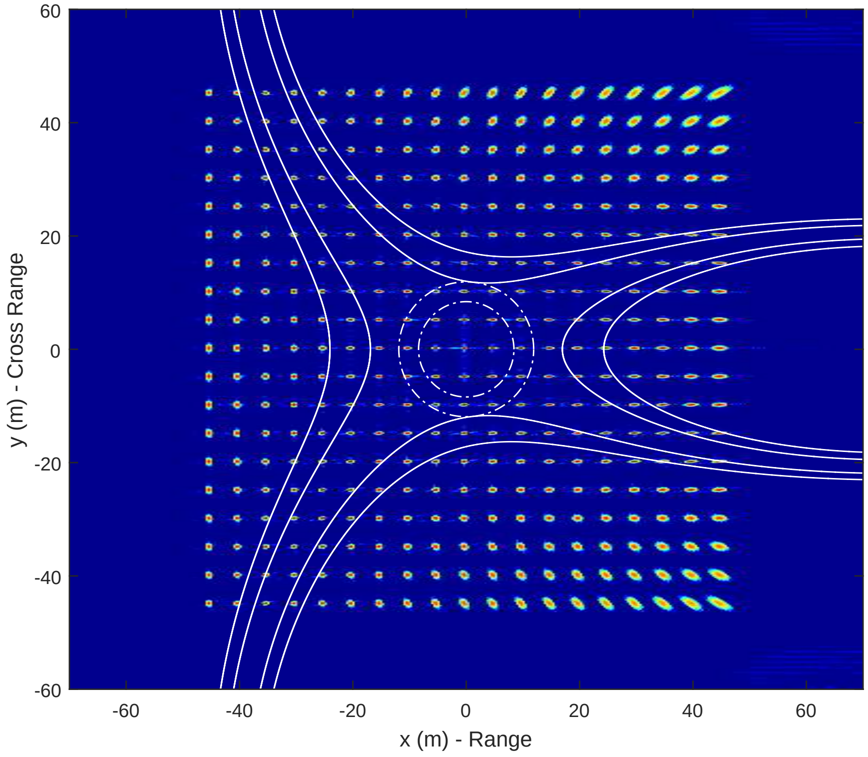

Figure 4.8: Comparison with previously published results - Linear flight path

These previous scene size limitations were all derived by analyzing the QPE terms without incorporating the accompanying distortion effects. They also assumed a linear flight path, which results in a planar collection geometry in the frequency space. However, if we look at the QPE term from [1] and apply the distortion correction, we arrive at a similar result as (4.25). (B.22) in [1] is the QPE requirement (in the notation of [1]):

$$\tilde{\Phi}_2 = \frac{x_0^{'2} - y_0^{'2}}{2r_0k_0} X_1^{'2} \leq \frac{\pi}{4} \tag{4.30}$$

According to [1], $X_1^{'} = \pi/\rho_a$, and $k_0 = 4\pi/\lambda$. Also, ${x_0}'$ and ${y_0}'$ denote the target location in the slant plane, and r_0 denotes the range to scene center. Note that in [1], y is range and x is cross range, and in this dissertation we use the opposite notation where x is range and y is cross range. If we also account for image distortion, then

$$ {x_0}' = \tilde{y} \tag{4.31}$$

$$ {x_0}' = \frac{r_{a0}}{r_{p0}} y \tag{4.32}$$

and

$$ {y_0}' = \tilde{x} \frac{x_a}{r_{a0}} \tag{4.33}$$

$$ {y_0}' = r_{a0} - rp0. \tag{4.34}$$

Substituting all these expressions into (4.30) gives

$$\tilde{\Phi}_2 = A \left(\frac{1}{r_{p0}} - \frac{2}{r_{a0}} - \frac{y^2}{r_{p0}^3} + \frac{r_{p0}}{r_{a0}^2} \right) \tag{4.35}$$

which exactly matches (4.25).

4.4 Chapter Summary

In this chapter, we described a novel approach for analyzing QPE in PFA. Analytic expressions were derived for the QPE for linear and circular flight paths, and the allowable scene size was determined for a well focused image. The QPE and scene size limitations were illustrated using point target simulations and for the large scene AFRL dataset. Finally, a comparison between results from this chapter and previously published works was presented.

The results derived here for the circular case will be used in the next section of the dissertation, where we derive an efficient correction algorithm, in Chapter 5.

Chapter 5

Fast PFA Correction Algorithm for Circular Flight Path

In this chapter, we present a novel algorithm which efficiently corrects a substantial amount of defocused regions in SAR imagery given circular flight paths. In Section 4.2.1, we derived the QPE for the circular case. For the large scene data example, we plotted the QPE in Figure 4.3 in image coordinates, and also plotted the QPE in Figure 4.4 in the distorted image coordinates. It appears from Figure 4.4 that a column of pixels in the distorted image coordinates has relatively constant QPE. Therefore, in this chapter we will investigate the feasibility of using a single QPE correction for an entire column of pixels in the distorted image coordinates. Such an approach would be computationally efficient as the correction would simply be applied as a complex multiplication in the range compressed image. For the unique case of a circular geometry, one may avoid the costly processing of spatially-varying post filtering [28, 30, 31]. Distortion due to QPE is corrected in the image domain after azimuth compression within PFA.

The remainder of this chapter is outlined as follows. Section 5.1 describes the new algorithm in detail. Section 5.2 analyzes the amount of QPE that is corrected in the new algorithm, and derives the residual QPE and scene size limitations for the AFRL Dataset.

Section 5.3.1 illustrates the new algorithm using the Point Target Scene. Section 5.3.2 shows the application of the new algorithm to the large scene AFRL Dataset, greatly increasing the focused scene size of the image. Finally, Section 5.4 details the computational requirements of the new algorithm and compares the computational efficiency with legacy algorithms. Most of the material from this chapter has been submitted for publication [37].

5.1 PFA Correction Algorithm Description

In Section 4.2.1, we derived the QPE terms for a circular flight path. In general, we can use these deterministic expressions as corrections which can be applied by a complex multiply in the phase history domain. However, these corrections vary across the undistorted image in both dimensions, and a brute force approach to applying the corrections is computationally expensive.

Since the distortion can be corrected by simply interpolating the image to a warped grid, we can use any of the available fast resampling algorithms [67–69, 122]. Here we focus on fast corrections for the QPE. For a circular flight path, the QPE varies predominantly with the range to the target and very little with the cross range distance in the distorted image coordinates, as seen in Figure 4.4. Therefore, we propose an algorithm where a single QPE correction is applied to an entire range gate of pixels before the azimuth FFT step in the PFA. This new correction permits defocus to be corrected with a simple series of range-dependent phase corrections, after range compression (i.e., FFTs) and before azimuth compression. This adds comparitively few computations to the process, and it corrects a significant amount of defocus, greatly increasing the focused scene size.

Figure 5.1 shows a block diagram of the new algorithm. The additional steps to PFA are depicted in brown. As in PFA, the incoming phase history, $S(f_k, \tau_n)$, is resampled onto a rectilinear grid, resulting in $S(f_x, f_y)$. We then perform the 1-D FFTs in range,

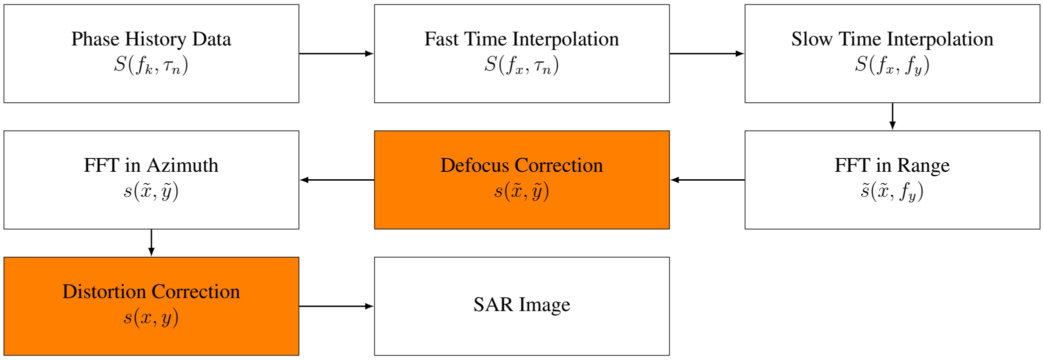

Figure 5.1: PFA correction algorithm block diagram

yielding a range-compressed image denoted as $\tilde{s}(\tilde{x}, f_y)$. It is here that we apply the defocus correction, which is dependent only on $\tilde{x}$. The correction is computed from (4.13), such that

$$\Phi_c(\tilde{x}) = -\tilde{\Phi}_2(\tilde{x}, y = 0) \tag{5.1}$$

$$= -A\left(\frac{x}{r_{p0}} - \frac{\tilde{x}}{r_a}\right) \tag{5.2}$$

Using (3.43), which is the distortion correction for the circular case derived in Section 3.3.2, we can solve for x in terms of $\tilde{x}$ for the special case of $y = 0$,

$$x = \tilde{x}\cos\theta_a + (x_{a0} - r_a). \tag{5.3}$$

Substituting (5.3) into (5.2) gives the QPE correction as a function of $\tilde{x}$,

$$\Phi_c(\tilde{x}) = -A\left(\frac{\tilde{x}\cos\theta_a + (x_{a0} - r_a)}{r_{p0}} - \frac{\tilde{x}}{r_a}\right). \tag{5.4}$$

where from (3.43),

$$r_{p0} = r_a - \tilde{x}\cos\theta_a. \tag{5.5}$$

Substituting (5.5) into (5.4) yields

$$\Phi_c(\tilde{x}) = A\left(1 + \frac{\tilde{x}}{r_a} - \frac{x_{a0}}{r_a - \tilde{x}\cos\theta_a}\right) \tag{5.6}$$

The correction is applied simply as

$$s(\tilde{x}, f_y) = \tilde{s}(\tilde{x}, f_y)e^{j\Phi_c(\tilde{x})t^2} \tag{5.7}$$

where the time interval $t \in [-1, 1]$ corresponds to the extent of f_y. Next we apply the same series of 1-D FFTs in azimuth, which results in a focused, but still distorted SAR image, denoted as $s(\tilde{x}, \tilde{y})$. Finally, we apply the distortion correction by resampling $s(\tilde{x}, \tilde{y})$ into $s(x, y)$ by using (3.43) and (3.44), resulting in the final corrected image.

5.2 Phase Error Analysis of Defocus Corrections

To illustrate the effectiveness of this new algorithm, we now analyze the resultant residual phase errors. For a given pixel in the image (x, y), the defocus correction is

$$\Phi_c = -A\left(\frac{\hat{x}}{r_{p0}} - \frac{\tilde{x}}{r_a}\right) \tag{5.8}$$

where $\hat{x}$ is the x coordinate at the $y = 0$ pixel that maps onto $\tilde{x}$ in (3.43). Solving for $\hat{x}$ in terms of x and y gives

$$\hat{x} = x_{a0} - \sqrt{(x - x_{a0})^2 + y^2}. \tag{5.9}$$

The correction, Φ_c, is applied to all pixels at a constant $\tilde{x}$, or to the arc of pixels in (x, y) which correspond to a given $\tilde{x}$. Therefore, the residual QPE after corrections is Φ_r, which is given as

$$
\begin{aligned}
\Phi_r &= \tilde{\Phi}_2 + \Phi_c & (5.10)\\
&= A\left(\frac{x}{r_{p0}} - \frac{\tilde{x}}{r_a} - \frac{y^2 x_{a0}}{r_{p0}^3}\right) - A\left(\frac{\hat{x}}{r_{p0}} - \frac{\tilde{x}}{r_a}\right) & (5.11)\\
&= A\left(\frac{x-\hat{x}}{r_{p0}} - \frac{y^2 x_{a0}}{r_{p0}^3}\right) & (5.12)
\end{aligned}
$$

using (4.13) and (5.8). Note that at $y = 0$, $\hat{x} = x$ and $\Phi_r = 0$. Therefore, all pixels in the center row of the image (corresponding to $y = 0$) are perfectly focused.

5.3 PFA Correction Algorithm Applications

Here we demonstrate the fast PFA correction algorithm on the two datasets: the Point Target Scene and the AFRL Dataset.

5.3.1 Point Target Scene

To illustrate the effects of defocus, we continue here with the Point Target Scene first developed in Section 2.5.1. Figure 2.2 depicts the locations of a grid of point targets which appear distorted and defocused in the PFA image in Figure 3.5. After applying the distortion correction, the targets appear in the correct location in Figure 3.6, but targets near the edges of the scene show significant defocus.

Here we apply the defocus correction as described in Section 5.1. The final image is displayed in Figure 5.2. The same contour lines of focus are again displayed, and they are again consistent with the pattern of degraded point responses in the corrected image. In this case, only the point targets in the upper right and lower right corners display significant defocus. The right part of the imaging region is closer to the sensor, so it is expected to have reduced focus at those extreme angles.

Figure 5.3 shows the residual QPE after the new correction algorithm is applied.

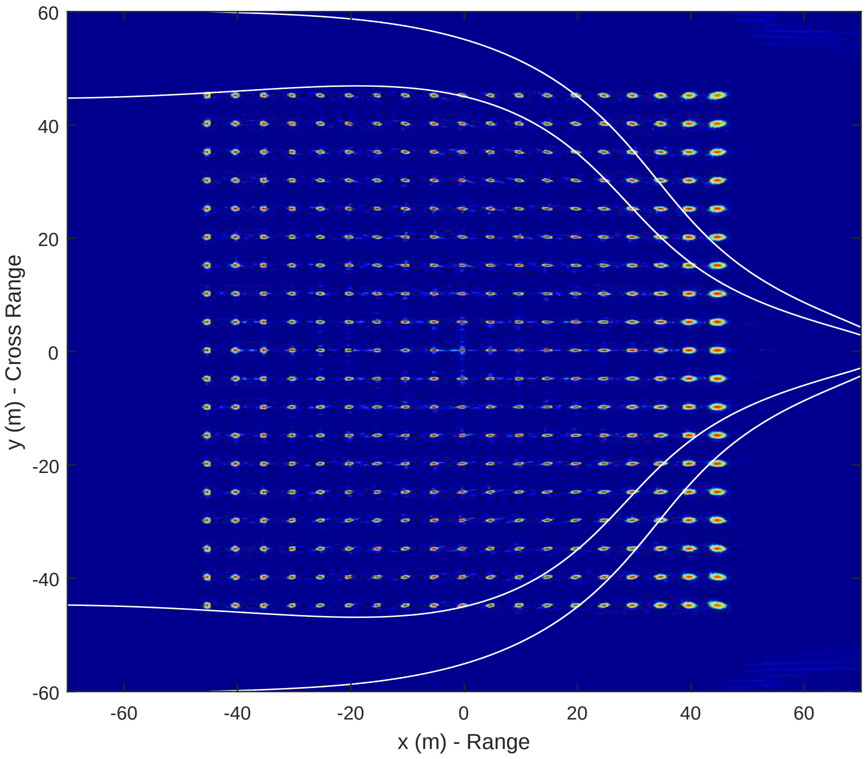

Figure 5.2: Point Target Scene with PFA correction algorithm

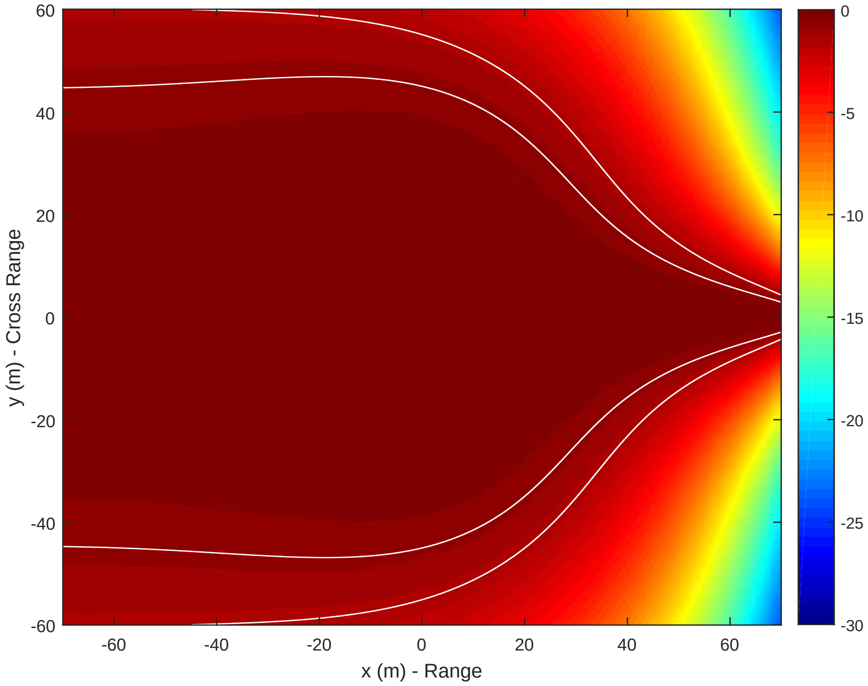

Figure 5.3: Residual QPE with PFA correction algorithm

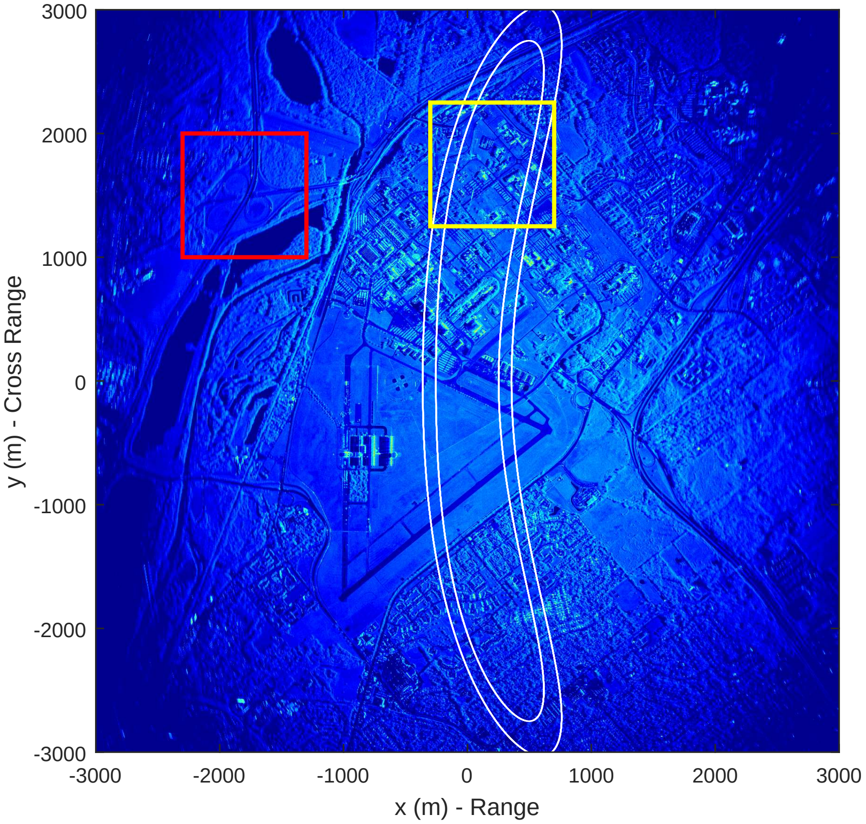

Figure 5.4: PFA Image with distortion correction - AFRL Dataset

5.3.2 AFRL Dataset

In this section, we will apply the new correction algorithm to the AFRL Dataset. In Section 3.3.2 we applied the circular distortion correction to the dataset. Figure 3.7 shows the original PFA image while Figure 3.8 shows the same image with the distortion correction applied. However, there is signficant defocus in the image. Figure 4.3 shows the residual QPE for the AFRL Dataset before corrections are applied.

Figure 5.4 again shows the PFA image with distortion correction applied, but we also add the contour lines of focus. From Section 4.2.1, only 11.5% of the image pixels are within the $\pi/2$ contour while 7.8% of the image pixels are within the $\pi/4$ contour.

It is unclear from the image that there is significant defocus in the image, so two regions are selected for closer examination. These regions are denoted by a yellow box and a red box. The yellow box depicts a region of the image that shows good focus while the

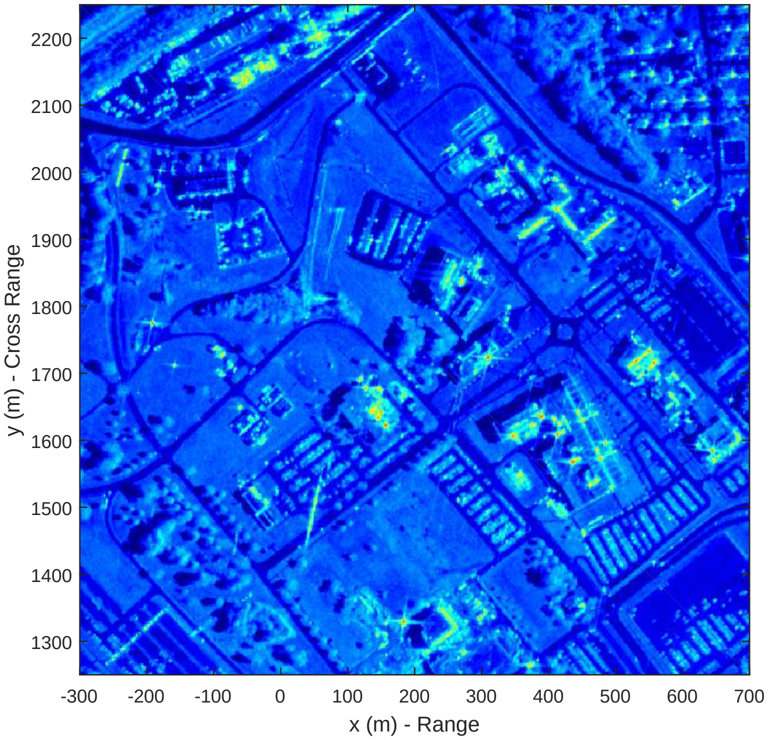

Figure 5.5: PFA Image - AFRL Dataset - Yellow Zoom Region

red box depicts a region of the image that shows poor focus. Figure 5.5 shows the yellow region zoomed in to clearly display the focused image. Figure 5.6 shows the red region zoomed in to clearly display the defocused part of the image.

Next, we apply the new algorithm described in Section 5.1 and the results are displayed in Figure 5.7. The same contour lines of focus are again displayed. The focused region of the image is significantly increased; 72.1$\%$ of the image pixels are within the $\pi/4$ contour (compared to 7.8% before corrections) and 85.0% of the image pixels are within the $\pi/2$ contour (compared to 11.5$\%$ before corrections). Figure 5.8 shows the residual QPE after the new algorithm.

Again we examine the two zoomed in regions. The yellow region is displayed in Figure 5.9, and this region is still well focused. The red region is displayed in Figure 5.10 and the impact of improved focus is readily apparent in the increased image contrast of the selected region.

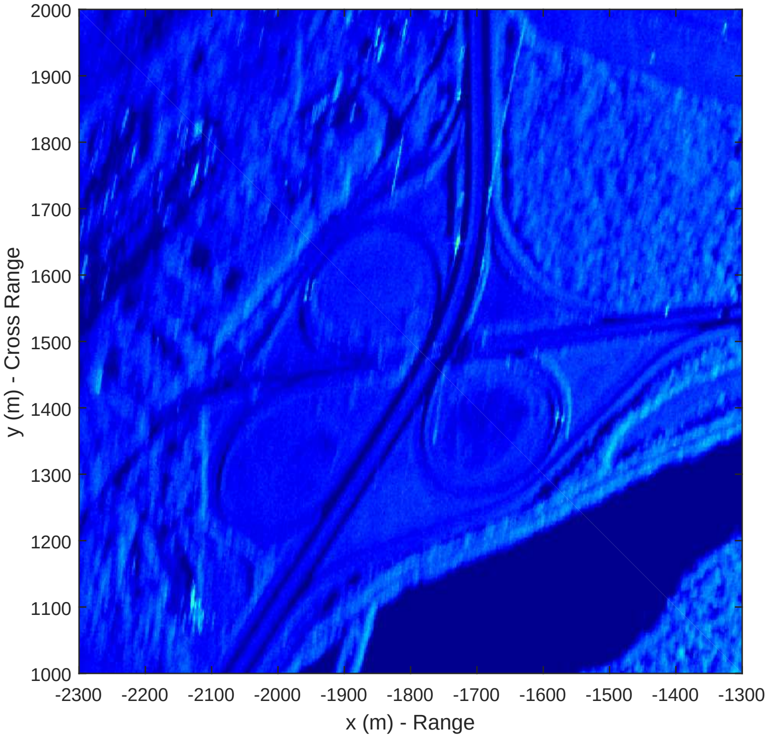

Figure 5.6: PFA Image - AFRL Dataset - Red Zoom Region

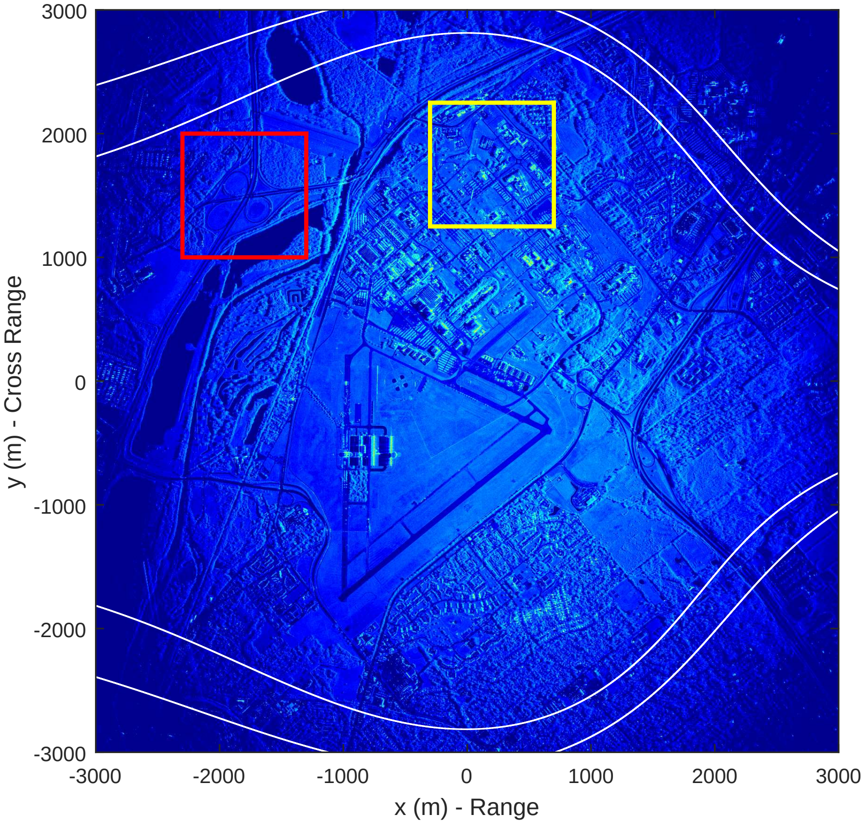

Figure 5.7: AFRL Dataset with PFA correction algorithm

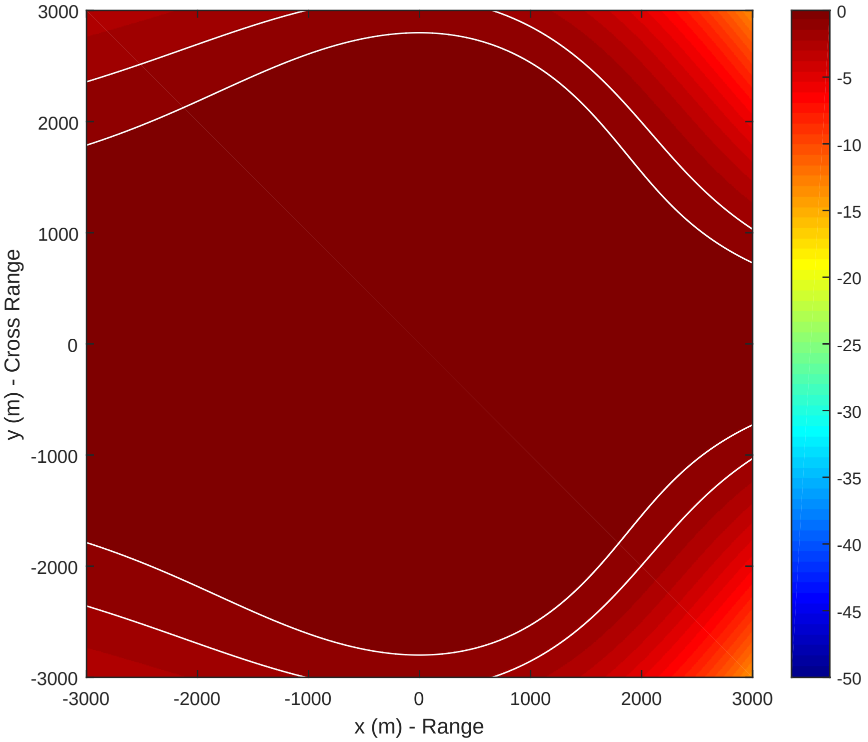

Figure 5.8: Residual QPE after defocus correction - AFRL Dataset

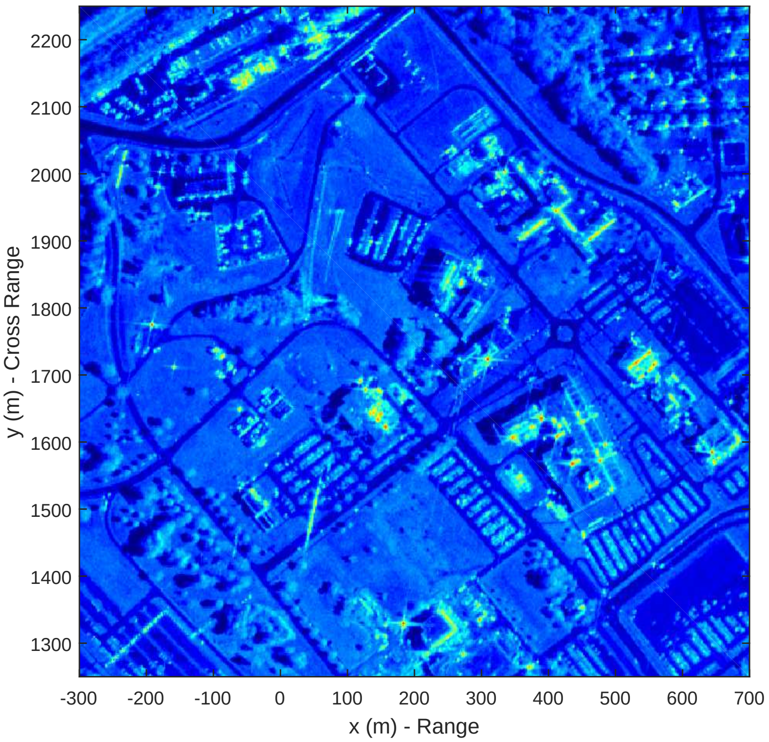

Figure 5.9: AFRL Dataset with PFA correction algorithm - Yellow Zoom Region

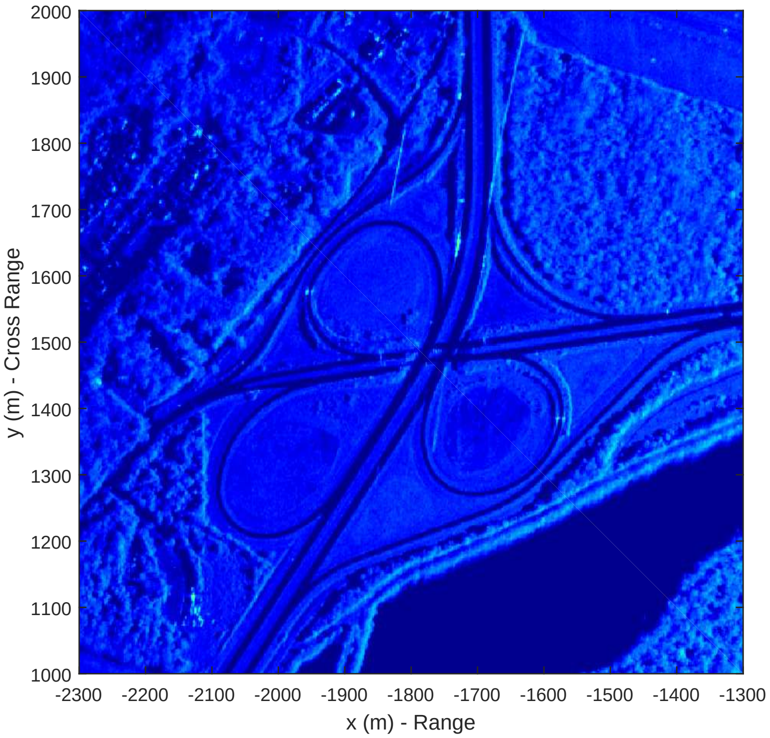

Figure 5.10: AFRL Dataset with PFA correction algorithm - Red Zoom Region

5.4 Computational Requirements for New Algorithm

In [27], the authors compared the computational complexity of different imaging algorithms in combination with a recursive spotlighting approach. Here, we will add our new algorithm to the comparisons. We start by defining the size of the input phase history to have N_p pulses, or slow time samples, each with K range gates, or fast time samples. In the two interpolation steps of PFA, we will interpolate to a slightly larger grid, N_x x N_y, which is chosen such that the FFT steps will perform efficiently. Ideally, N_x and N_y should have values that are powers of two.

The interpolations require 175 computations per output sample, so the "fast time" interpolation uses $175 N_p N_x$ operations and the "slow time" interpolation uses $175 N_y N_x$ operations. We assume that a length-N FFT requires $5N \log_2 N$ computations, so the 1-D FFTs in range use $5 N_y N_x \log_2 N_x$ computations (since there are N_y FFTs of length N_x) and the 1-D FFTs in azimuth use $5 N_x N_y \log_2 N_y$ computations (since there are N_x FFTs of length N_y).

The correction algorithm adds two additional computation steps. The first is the defocus correction, which is implemented by a complex multiplication of every sample with the calculated phase correction. Since a complex multiplication requires six operations, this step uses $6N_yN_x$ computations. The second is a resampling of the final image, which includes the distortion correction, and we conservatively assume that this step will have the same requirements as the other interpolations, namely 175 computations per output sample in each direction, yielding $350N_xN_y$ computations. Other resampling algorithms may have fewer computations, such as the bilinear interpolation which requires about 100 computations for every complex output sample.

The AFRL Dataset has $K = 21232$ and $N_p = 30000$ input samples, and values of $N_x = 24576$ and $N_y = 36864$ were chosen for efficient FFT computation. Using the above assumptions, we estimate that the original PFA image uses 422.4 GFlops of computations. The defocus corrections add 5.4 GFlops and the distortion correction adds 317.1 GFlops, so the total corrected algorithm requires 744.9 GFlops.

In comparison, the spotlighted PFA described in [27] requires 1,725.8 GFlops while the spotlighted BPA described in the same paper requires 5,597 GFlops for this dataset, using equations derived in [27]. Therefore, the new algorithm requires only 43.2% of the computations of the spotlighted PFA algorithm and only 13.3% of the computations of the spotlighted BPA, while yielding a distortion-free image with 85% of the pixels well focused.

5.5 Chapter Summary

In this chapter, we derived and demonstrated a new fast algorithm for forming large scene SAR images with a circular flight path. We utilized previous derivations of linear and QPEs to derive corrections for the PFA image. A single QPE correction is applied between the range FFT step and the azimuth FFT step of PFA, resulting in a significantly larger focused scene size. Also, a distortion correction is applied utilizing a 2-D interpolation, yielding a distortion free image.

This algorithm was demonstrated using the Point Target Scene and also the large scene measured AFRL dataset. Finally, the computational requirements of the new algorithm were described and compared with other algorithms.

Chapter 6

Closing Remarks

In this chapter, we provide a summary of the unique contributions of this dissertation, discuss expected impacts, and provide some thoughts about future research in this area.

6.1 Summary of Contributions

This dissertation includes three significant contributions, culminating in a new computationally efficient image formation algorithm for circular flight paths that corrects for distortion and defocus artifacts.

First, we employ a new method for phase error analysis by using a Taylor Expansion in the temporal dimension. This allows for more accurate isolation of the constant, linear and quadratic phase error terms for any arbitrary flight path. The Taylor Expansion is used to derive closed-form analytic expressions for constant, linear and quadratic phase errors.

Second, we use this phase error analysis to accurately determine scene size limitations for PFA. By including the distortion correction as part of the QPE analysis, the resulting scene size limitations are notably different from the circular regions of focus determined in earlier works. In particular, we determined regions of focus that are arbitrary in shape to include all areas in the image with acceptable focus.

Finally, we derived a new fast algorithm which corrects for both distortion and defocus for a circular flight path. The algorithm adds two processing steps to PFA, but it adds compartively few computations to the overall imaging process while correcting a significant amount of defocus, and therefore greatly increasing the focused scene size. This algorithm is demonstrated on point target simulations and a measured large scene dataset.

6.2 Expected Impact

This dissertation provides a novel way of analyzing phase errors in PFA images. Providing accurate isolation of constant, linear, and quadratic phase errors allows for the development of accurate distortion corrections and efficient defocus correction algorithms. In particular, a fast algorithm for implementing defocus corrections for circular flight paths is presented.

This fast algorithm results in a significant increase in allowable scene size, enabling the collection of larger SAR scenes with modest increases in computational complexity. In particular, this fast algorithm applicable to circular flight paths will benefit wide area, staring SAR sensors which offer unique exploitation capabilities over these larger SAR scenes.

6.3 Future Research

The phase error analysis presented here provides a good theoretical foundation for future research in PFA correction algorithms. For instance, this analysis was used to derive a correction algorithm for a linear flight path with squinted geometries [123].

In the future, correction algorithms can be derived for other types of flight paths such as quadratic and elliptical flight paths, and also numerous types of squinted geometries. The phase error analysis can also be extended to bi-static SAR operations.

Bibliography

[1] C. V. Jakowatz, D. E. Wahl, P. H. Eichel, D. C. Ghiglia, and P. A. Thompson, *Spotlight-mode synthetic aperture radar: a signal processing approach.* Kluwer Academic Publishers Norwell, MA, 1996, vol. 101.

[2] J. C. Curlander and R. N. McDonough, *Synthetic Aperture Radar: Systems and Signal Processing*, 1st ed. Wiley-Interscience, 11 1991.

[3] W. T. K. Johnson, "Magellan imaging radar mission to Venus," *Proceedings of the IEEE*, vol. 79, no. 6, pp. 777–790, Jun 1991.

[4] M. Chen, T. Cheng, and M. Jin, "Magellan SAR Processing Algorithm And H/w Design," in *Geoscience and Remote Sensing Symposium, 1989. IGARSS'89. 12th Canadian Symposium on Remote Sensing., 1989 International*, vol. 3, Jul 1989, pp. 1707–1712.

[5] C. A. Wiley, "Pulsed doppler radar methods and apparatus," Jul. 20 1965, US Patent 3,196,436.

[6] L. J. Cutrona, E. N. Leith, C. J. Palermo, and L. J. Porcello, "Optical data processing and filtering systems," *Information Theory, IRE Transactions on*, vol. 6, no. 3, pp. 386–400, 1960.

[7] W. M. Brown and L. J. Porcello, “An introduction to synthetic-aperture radar,” *Spectrum, IEEE*, vol. 6, no. 9, pp. 52–62, Sept 1969.

[8] J. Kirk, J.C., “A discussion of digital processing in synthetic aperture radar,” *Aerospace and Electronic Systems, IEEE Transactions on*, vol. AES-11, no. 3, pp. 326–337, May 1975.

[9] E. Hayden, M. Schmalz, W. Chapman, S. Ranka, S. Sahni, and G. Seetharaman, “Techniques for mapping synthetic aperture radar processing algorithms to multi-GPU clusters,” in *Signal Processing and Information Technology (ISSPIT), 2012 IEEE International Symposium on*, Dec 2012, pp. 000 013–000 018.

[10] M. Desai and W. Jenkins, “Convolution backprojection image reconstruction for spotlight mode synthetic aperture radar,” *Image Processing, IEEE Transactions on*, vol. 1, no. 4, pp. 505–517, 1992.

[11] D. Munson Jr, J. O’Brien, and W. Jenkins, “A tomographic formulation of spotlight-mode synthetic aperture radar,” *Proceedings of the IEEE*, vol. 71, no. 8, pp. 917–925, 1983.

[12] W. Carrara, R. Goodman, and R. Majewski, *Spotlight synthetic aperture radar: Signal processing algorithms*. Artech House (Boston), 1995.

[13] L. A. Gorham and L. J. Moore, “SAR image formation toolbox for MATLAB,” in *Society of Photo-Optical Instrumentation Engineers (SPIE) Conference Series*, vol. 7699, Apr. 2010.

[14] M. Soumekh, *Synthetic aperture radar signal processing with MATLAB algorithms*. Wiley-Interscience, 1999.

[15] M. L. Bryant, “Multisensor staring exploitation,” in *SPIE Defense and Security Symposium*. International Society for Optics and Photonics, 2008, pp. 69 810J–69 810J.

[16] R. L. Moses, L. C. Potter, and M. Cetin, “Wide-angle SAR imaging,” in *Defense and Security*. International Society for Optics and Photonics, 2004, pp. 164–175.

[17] L. Moore, J. Parker, L. Gorham, U. Majumder, M. Minardi, and S. Scarborough, “Staring RF signal processing challenges,” in *Electromagnetics in Advanced Applications (ICEAA), 2011 International Conference on*, Sept 2011, pp. 279–282.

[18] J. Kirk, S. Darden, U. Majumder, and S. Scarborough, “Forty years of digital SAR and slow GMTI technology,” in *Radar Conference, 2014 IEEE*, May 2014, pp. 0064–0069.

[19] M. Saville, J. Jackson, and D. Fuller, “Rethinking vehicle classification with wide-angle polarimetric SAR,” *Aerospace and Electronic Systems Magazine, IEEE*, vol. 29, no. 1, pp. 41–49, Jan 2014.

[20] K. Dungan and J. Nehrbass, “Wide-area wide-angle SAR focusing,” *Aerospace and Electronic Systems Magazine, IEEE*, vol. 29, no. 1, pp. 21–28, Jan 2014.

[21] K. E. Dungan and L. C. Potter, “3-D imaging of vehicles using wide aperture radar,” *Aerospace and Electronic Systems, IEEE Transactions on*, vol. 47, no. 1, pp. 187–200, 2011.

[22] C. Paulson and E. Zelnio, “The effect of SAR imaging conditions on classification algorithms,” in *Radar Conference, 2014 IEEE*, May 2014, pp. 0906–0911.

[23] A. Rogan and R. Carande, “Improving the fast back projection algorithm through massive parallelizations,” in *SPIE Defense, Security, and Sensing*. International Society for Optics and Photonics, 2010, pp. 76 690I–76 690I.

[24] C. Usmail, M. Little, and R. Zuber, “Evolution of embedded processing for wide area surveillance,” *Aerospace and Electronic Systems Magazine, IEEE*, vol. 29, no. 1, pp. 6–13, Jan 2014.

[25] T. M. Benson, D. P. Campbell, and D. A. Cook, “Gigapixel spotlight synthetic aperture radar backprojection using clusters of GPUs and CUDA,” in *Radar Conference (RADAR), 2012 IEEE*. IEEE, 2012, pp. 0853–0858.

[26] M. Soumekh, “Digital spotlighting and coherent subaperture image formation for stripmap synthetic aperture radar,” in *Image Processing, 1994. Proceedings. ICIP-94., IEEE International Conference*, vol. 1. IEEE, 1994, pp. 476–480.

[27] B. Rigling, W. Garber, R. Hawley, and L. Gorham, “Wide-area, persistent SAR imaging: Algorithm tradeoffs,” *Aerospace and Electronic Systems Magazine, IEEE*, vol. 29, no. 1, pp. 14–20, 2014.

[28] N. E. Doren, J. Jakowatz, C. V., D. E. Wahl, and P. A. Thompson, “General formulation for wavefront curvature correction in polar-formatted spotlight-mode SAR images using space-variant post-filtering,” in *Image Processing, 1997. Proceedings., International Conference on*, vol. 1, 1997, pp. 861–864.

[29] B. Rigling and R. Moses, “Taylor expansion of the differential range for monostatic SAR,” *Aerospace and Electronic Systems, IEEE Transactions on*, vol. 41, no. 1, pp. 60–64, 2005.

[30] N. Doren, “Space-variant post-filtering for wavefront curvature correction in polar-formatted spotlight-mode SAR imagery,” Sandia National Labs., Albuquerque, NM (US); Sandia National Labs., Livermore, CA (US), Tech. Rep., 1999.

[31] W. L. Garber and R. W. Hawley, “Extensions to polar formatting with spatially variant post-filtering,” in *SPIE Defense, Security, and Sensing*. International Society for Optics and Photonics, 2011, pp. 805 104–805 104.

[32] L. A. Gorham and B. D. Rigling, “Scene size limits for polar format algorithm,” *IEEE Transactions on Aerospace and Electronic Systems*, 2015, to be published.

[33] M. Horvath, L. Gorham, and B. D. Rigling, “Scene size bounds for PFA imaging with postfiltering,” *Aerospace and Electronic Systems, IEEE Transactions on*, vol. 49, no. 2, pp. 1402–1406, 2013.

[34] J. Walker, “Range-doppler imaging of rotating objects,” *Aerospace and Electronic Systems, IEEE Transactions on*, vol. 1, no. 1, pp. 23–52, 1980.

[35] A. W. Doerry, *Wavefront curvature limitations and compensation to polar format processing for synthetic aperture radar images*. United States. Department of Energy, 2006.

[36] S. Demirci, E. Yigit, and C. Ozdemir, “Wide-field circular SAR imaging: An empirical assessment of layover effects,” *Microwave and Optical Technology Letters*, vol. 57, no. 2, pp. 489–497, 2015. [Online]. Available: http://dx.doi.org/10.1002/mop.28884

[37] L. A. Gorham and B. D. Rigling, “Fast corrections for polar format algorithm with a circular flight trajectory,” *IEEE Transactions on Aerospace and Electronic Systems*, 2015, submitted for publication.

[38] L. A. Gorham, U. K. Majumder, P. Buxa, M. J. Backues, and A. C. Lindgren, “Implementation and analysis of a fast backprojection algorithm,” in *Society of Photo-Optical Instrumentation Engineers (SPIE) Conference Series*, vol. 6237, Jun. 2006.

[39] L. A. Gorham, B. D. Rigling, and E. G. Zelnio, “A comparison between imaging radar and medical imaging polar format algorithm implementations,” in *Society of Photo-Optical Instrumentation Engineers (SPIE) Conference Series*, vol. 6568, Apr. 2007.

[40] L. A. Gorham and B. D. Rigling, “Dual format algorithm for monostatic SAR,” in *Proceedings of SPIE*, vol. 7699, 2010, p. 769905.

[41] L. A. Gorham and B. D. Rigling, “Dual format algorithm implementation with gotcha data,” in *SPIE Defense, Security, and Sensing*. International Society for Optics and Photonics, 2012, pp. 839 403–839 403.

[42] Air Force Research Laboratory (AFRL), “Large Scene Gotcha Data Example,” Sensor Data Management System (SDMS). [Online]. Available: https://www.sdms.afrl.af.mil/

[43] G. Franceschetti and R. Lanari, *Synthetic aperture radar processing*. CRC press, 1999.

[44] I. G. Cumming and F. H.-c. Wong, *Digital processing of synthetic aperture radar data: algorithms and implementation*. Artech House, 2005.

[45] M. A. Richards, *Fundamentals of radar signal processing*. Tata McGraw-Hill Education, 2005.

[46] R. J. Sullivan, *Microwave radar: Imaging and advanced concepts*. Artech House (Boston), 2000.

[47] A. W. Rihaczek and S. J. Hershkowitz, *Radar Resolution and Complex-Image Analysis*. Artech House Publishers, 1996.

[48] A. Hein, *Processing of SAR data: fundamentals, signal processing, interferometry*. Springer, 2004.

[49] C. Cook, *Radar signals: An introduction to theory and application*. Elsevier, 2012.

[50] C. Sherwin, J. Ruina, and R. Rawcliffe, “Some early developments in synthetic aperture radar systems,” *Military Electronics, IRE Transactions on*, vol. 1051, no. 2, pp. 111–115, 1962.

[51] C. Elachi, T. Bicknell, R. Jordan, and C. Wu, "Spaceborne synthetic-aperture imaging radars: Applications, techniques, and technology," *Proceedings of the IEEE*, vol. 70, no. 10, pp. 1174–1209, 1982.

[52] P. A. Rosen, S. Hensley, I. R. Joughin, F. K. Li, S. N. Madsen, E. Rodriguez, and R. M. Goldstein, "Synthetic aperture radar interferometry," *Proceedings of the IEEE*, vol. 88, no. 3, pp. 333–382, 2000.

[53] A. Reigber, R. Scheiber, M. Jager, P. Prats-Iraola, I. Hajnsek, T. Jagdhuber, K. Papathanassiou, M. Nannini, E. Aguilera, S. Baumgartner, R. Horn, A. Nottensteiner, and A. Moreira, "Very-High-Resolution Airborne Synthetic Aperture Radar Imaging: Signal Processing and Applications," *Proceedings of the IEEE*, vol. 101, no. 3, pp. 759–783, March 2013.

[54] W. Brown and R. Fredricks, "Range-doppler imaging with motion through resolution cells," *Aerospace and Electronic Systems, IEEE Transactions on*, vol. AES-5, no. 1, pp. 98 –102, jan. 1969.

[55] W. Caputi, "Stretch: A time-transformation technique," *Aerospace and Electronic Systems, IEEE Transactions on*, vol. AES-7, no. 2, pp. 269–278, March 1971.

[56] A. W. Doerry, "Basics of polar-format algorithm for processing synthetic aperture radar images," *Sandia National Laboratories report SAND2012-3369, Unlimited Release*, 2012.

[57] D. Zhu, S. Ye, and Z. Zhu, "Polar format agorithm using chirp scaling for spotlight SAR image formation," *Aerospace and Electronic Systems, IEEE Transactions on*, vol. 44, no. 4, pp. 1433–1448, Oct 2008.

[58] Q. Liu, W. Hong, W. Tan, Y. Lin, Y. Wang, and Y. Wu, "An improved polar format algorithm with performance analysis for geosynchronous circular SAR 2D imaging," *Progress In Electromagnetics Research*, vol. 119, pp. 155–170, 2011.

[59] R. Crochiere and L. Rabiner, “Interpolation and decimation of digital signals: A tutorial review,” *Proceedings of the IEEE*, vol. 69, no. 3, pp. 300–331, 1981.

[60] D. Munson Jr, J. Sanz, W. Jenkins, G. Kakazu, and B. Mather, “A comparison of algorithms for polar-to-cartesian interpolation in spotlight mode SAR,” in *Acoustics, Speech, and Signal Processing, IEEE International Conference on ICASSP’85.*, vol. 10. IEEE, 1985, pp. 1364–1367.

[61] J. O’Sullivan, “A fast sinc function gridding algorithm for fourier inversion in computer tomography,” *Medical Imaging, IEEE Transactions on*, vol. 4, no. 4, pp. 200–207, 1985.

[62] J. Jackson, C. Meyer, D. Nishimura, and A. Macovski, “Selection of a convolution function for fourier inversion using gridding [computerised tomography application],” *Medical Imaging, IEEE Transactions on*, vol. 10, no. 3, pp. 473–478, 1991.

[63] Y. Kadah, “New solution to the gridding problem,” in *Proc. SPIE*, vol. 4684, 2002, p. 2.

[64] D. Noll and B. Sutton, “Gridding procedures for non-cartesian k-space trajectories,” in *11th Scientific Meeting, Int. Society of Magnetic Resonance in Med., Toronto*. Citeseer, 2003.

[65] A. W. Doerry, E. Bishop, J. Miller, V. Horndt, and D. Small, “Designing interpolation kernels for SAR data resampling,” in *Proceedings of SPIE*, vol. 8361, 2012.

[66] R. Deming, M. Best, and S. Farrell, “Polar format algorithm for SAR imaging with MATLAB,” in *SPIE Defense+ Security*. International Society for Optics and Photonics, 2014, pp. 909 306–909 306.

[67] G. Beylkin, J. Gorman, S. Li-Fliss, and M. Ricoy, “SAR imaging and multiresolution analysis,” in *Proceedings of SPIE*, vol. 2487, 1995, p. 144.

[68] Y. Wang, J. Li, J. Chen, H. Xu, and B. Sun, "A novel non-interpolation polar format algorithm using non-lineal flight trajectories and auto-adaptive PRF technique," *Progress In Electromagnetics Research*, vol. 122, pp. 155–173, 2012.

[69] B. Fan, J. Wang, Y. Qin, H. Wang, and H. Xiao, "Polar format algorithm based on fast gaussian grid non-uniform fast fourier transform for spotlight synthetic aperture radar imaging," *Radar, Sonar Navigation, IET*, vol. 8, no. 5, pp. 513–524, June 2014.

[70] R. Mersereau and A. Oppenheim, "Digital reconstruction of multidimensional signals from their projections," *Proceedings of the IEEE*, vol. 62, no. 10, pp. 1319–1338, 1974.

[71] H. Stark, J. Woods, I. Paul, and R. Hingorani, "An investigation of computerized tomography by direct fourier inversion and optimum interpolation," *Biomedical Engineering, IEEE Transactions on*, vol. 7, no. 7, pp. 496–505, 1981.

[72] C. Jakowatz and P. Thompson, "A new look at spotlight mode synthetic aperture radar as tomography: imaging 3D targets," *Image Processing, IEEE Transactions on*, vol. 4, no. 5, pp. 699–703, 1995.

[73] M. Cetin and W. Karl, "A statistical tomographic approach to synthetic aperture radar image reconstruction," in *Image Processing, 1997. Proceedings., International Conference on*, vol. 1. IEEE, 1997, pp. 845–848.

[74] J. McCorkle and M. Rofheart, "An order N^2log(N) backprojector algorithm for focusing wide-angle widebandwidth arbitrary-motion synthetic aperture radar," in *Proc. of SPIE Conference on Radar Sensor Technology*, vol. 2747, 1996, pp. 25–36.

[75] A. Yegulalp, "Fast backprojection algorithm for synthetic aperture radar," in *Radar Conference, 1999. The Record of the 1999 IEEE.* IEEE, 1999, pp. 60–65.

[76] R. Lee, J. Verdi, and M. Soumekh, “Enhancements of NP-3 UHF image quality using digital spotlighting technique,” in *Radar Conference, 2001. Proceedings of the 2001 IEEE.* IEEE, 2001, pp. 1–6.

[77] L. Nguyen, M. Ressler, D. Wong, and M. Soumekh, “Enhancement of backprojection SAR imagery using digital spotlighting preprocessing,” in *Radar Conference, 2004. Proceedings of the IEEE.* IEEE, 2004, pp. 53–58.

[78] K. E. Dungan, L. A. Gorham, and L. J. Moore, “SAR digital spotlight implementation in matlab,” in *SPIE Defense, Security, and Sensing.* International Society for Optics and Photonics, 2013, pp. 87 460A–87 460A.

[79] Z. Yang, M. Xing, Y. D. Zhang, G. Sun, and Z. Bao, “Factorised polar-format backprojection algorithm,” *IET Radar, Sonar & Navigation*, vol. 9, pp. 875–880(5), August 2015.

[80] J. Torgrimsson, P. Dammert, H. Hellsten, and L. M. Ulander, “Autofocus and analysis of geometrical errors within the framework of fast factorized back-projection,” in *SPIE Defense+ Security.* International Society for Optics and Photonics, 2014, pp. 909 303–909 303.

[81] C. Prati and V. Rampa, “Real-time parallel processor for on-board airborne synthetic aperture radar SAR,” in *Circuits and Systems, 1990., IEEE International Symposium on*, May 1990, pp. 2905–2908 vol.4.

[82] P. Buxa, L. Gorham, M. Lukacs, and D. Caliga, “Mapping of a 2D SAR Backprojection Algorithm to an SRC Reconfigurable Computing MAP Processor,” in *Ninth Annual Workshop on High Performance Embedded Computing*, MIT Lincoln Laboratory, Ed., 2005.

[83] D. Fan, “Implementation of a power efficient synthetic aperture radar back projection algorithm on FPGAs using OpenCL,” Ph.D. dissertation, University of Dayton, 2015.

[84] D. Pritsker, “Efficient global back-projection on an FPGA,” in *Radar Conference (RadarCon), 2015 IEEE*, May 2015, pp. 0204–0209.

[85] M. Di Bisceglie, M. Di Santo, C. Galdi, R. Lanari, and N. Ranaldo, “Synthetic aperture radar processing with GPGPU,” *Signal Processing Magazine, IEEE*, vol. 27, no. 2, pp. 69–78, March 2010.

[86] F. Kraja, A. Murarasu, G. Acher, and A. Bode, “Performance evaluation of SAR image reconstruction on CPUs and GPUs,” in *Aerospace Conference, 2012 IEEE*, March 2012, pp. 1–16.

[87] T. Hartley, A. Fasih, C. Berdanier, F. Özgüner, and U. Çatalyürek, “Investigating the use of GPU-accelerated nodes for SAR image formation,” in *Cluster Computing and Workshops, 2009. CLUSTER ’09. IEEE International Conference on*, Aug 31–Sep 4 2009, pp. 1–8.

[88] D. Wang and M. Ali, “Synthetic aperture radar on low power multi-core digital signal processor,” in *High Performance Extreme Computing (HPEC), 2012 IEEE Conference on*, Sept 2012, pp. 1–6.

[89] F. Rocca, C. Cafforio, and C. Prati, “Synthetic aperture radar: A new application for wave equation techniques,” *Geophysical prospecting*, vol. 37, no. 7, pp. 809–830, 1989.

[90] C. Cafforio, C. Prati, and F. Rocca, “SAR data focusing using seismic migration techniques,” *Aerospace and Electronic Systems, IEEE Transactions on*, vol. 27, no. 2, pp. 194–207, 1991.

[91] C. Prati, A. M. Guarnieri, and F. Rocca, “Spot mode SAR focusing with the WK technique,” in *IGARSS*, vol. 2, 1991, pp. 631–634.

[92] Z. Li, J. Wang, and Q. H. Liu, “Interpolation-free stolt mapping for SAR imaging,” *Geoscience and Remote Sensing Letters, IEEE*, vol. 11, no. 5, pp. 926–929, May 2014.

[93] G. Nash, U. Cheema, R. Ansari, and A. Khokhar, “Power-efficient RMA SAR imaging using pipelined non-uniform fast fourier transform,” in *Radar Conference (RadarCon), 2015 IEEE*, May 2015, pp. 1600–1604.

[94] R. Bamler, “A comparison of range-doppler and wavenumber domain SAR focusing algorithms,” *Geoscience and Remote Sensing, IEEE Transactions on*, vol. 30, no. 4, pp. 706–713, Jul 1992.

[95] C. Chang, M. Jin, and J. Curlander, “SAR processing based on the exact two-dimensional transfer function,” in *Geoscience and Remote Sensing Symposium, 1992. IGARSS ’92. International*, vol. 1, May 1992, pp. 355–359.

[96] C. V. Jakowatz, P. A. Thompson, and D. E. Wahl, “Performance of the polar formatting algorithm for SAR image formation on wide aperture collections,” 2000.

[97] Y. Na, H. Sun, Y.-H. Lee, L. C. Tai, and H. L. Chan, “Performance evaluation of back-projection and range migration algorithms in foliage penetration radar imaging,” in *Image Processing, 2004. ICIP ’04. 2004 International Conference on*, vol. 1, Oct 2004, pp. 21–24 Vol. 1.

[98] C. Jakowatz Jr, D. Wahl, D. Yocky, B. Bray, W. Bow Jr, and J. Richards, “Comparison of algorithms for use in real-time spotlight-mode SAR image formation,” in *Proceedings of SPIE*, vol. 5427, 2004, p. 108.

[99] X. Mao, D.-Y. Zhu, L. Ding, and Z.-D. Zhu, “Comparative study of RMA and PFA on their responses to moving target,” *Progress In Electromagnetics Research*, vol. 110, pp. 103–124, 2010.

[100] J. R. Cruz, “Comparison of image processing techniques using random noise radar,” DTIC Document, Tech. Rep., 2014.

[101] J. Fienup, “Detecting moving targets in SAR imagery by focusing,” *Aerospace and Electronic Systems, IEEE Transactions on*, vol. 37, no. 3, pp. 794–809, July 2001.

[102] G. Zeoli, “The effect of constant velocity error on SAR focus,” *Aerospace and Electronic Systems, IEEE Transactions on*, vol. AES-22, no. 5, pp. 657–659, Sept 1986.

[103] G. Fornaro, E. Sansosti, R. Lanari, and M. Tesauro, “Role of processing geometry in SAR raw data focusing,” *Aerospace and Electronic Systems, IEEE Transactions on*, vol. 38, no. 2, pp. 441–454, Apr 2002.

[104] H. Xie, H. Zhao, and Q. Fu, “Taylor expansion and its application in missile-borne SAR imaging,” in *Proc. 2nd Asian-Pacific Conf. Synthetic Aperture Radar APSAR 2009*, 2009, pp. 426–430.

[105] C. Musgrove, “Polar Format Algorithm: Survey of Assumptions and Approximations,” Sandia National Labs., Albuquerque, NM (US); Sandia National Labs., Livermore, CA (US), Tech. Rep., 2012.

[106] D. Zhu, X. Mao, Y. Li, and Z. Zhu, “Derivation of the far-field limit of PFA for SAR moving target imaging,” in *Radar Conference, 2009 IET International*, April 2009, pp. 1–5.

[107] ——, “Far-field limit of PFA for SAR moving target imaging,” *Aerospace and Electronic Systems, IEEE Transactions on*, vol. 46, no. 2, pp. 917–929, April 2010.

[108] C. Lawyer and B. Rigling, “Automatic target recognition driven scene size limits for the polar format algorithm,” in *Radar Conference, 2014 IEEE*, May 2014, pp. 0813–0818.

[109] F. Berizzi, G. Corsini, M. Diani, and M. Veltroni, “Autofocus of wide azimuth angle SAR images by contrast optimisation,” in *Geoscience and Remote Sensing Symposium, 1996. IGARSS’96.’Remote Sensing for a Sustainable Future.’, International*, vol. 2. IEEE, 1996, pp. 1230–1232.

[110] C. Jakowatz Jr, D. Wahl, P. Thompson, and N. Doren, “Space-variant filtering for correction of wavefront curvature effects in spotlight-mode SAR imagery formed via polar formatting,” in *Proceedings of SPIE*, vol. 3070, 1997, p. 33.

[111] M. Preiss, D. Gray, and N. Stacy, “Space variant filtering of polar format spotlight SAR images for wavefront curvature correction and interferometric processing,” in *Proc. IEEE Int. Geoscience and Remote Sensing Symp. IGARSS ’02*, vol. 1, 2002, pp. 179–181.

[112] X. Mao, D. Zhu, and Z. Zhu, “Polar format algorithm wavefront curvature compensation under arbitrary radar flight path,” in *Radar (Radar), 2011 IEEE CIE International Conference on*, vol. 2, Oct 2011, pp. 1382–1385.

[113] ——, “Polar format algorithm wavefront curvature compensation under arbitrary radar flight path,” *Geoscience and Remote Sensing Letters, IEEE*, vol. 9, no. 3, pp. 526–530, May 2012.

[114] X. Peng, W. Hong, Y. Wang, W. Tan, and Y. Wu, “Polar format imaging algorithm with wave-front curvature phase error compensation for airborne DLSLA three-dimensional SAR,” *Geoscience and Remote Sensing Letters, IEEE*, vol. 11, no. 6, pp. 1036–1040, June 2014.

[115] W. Carrara, R. Goodman, and M. Ricoy, “New algorithms for widefield SAR image formation,” in *Radar Conference, 2004. Proceedings of the IEEE*, April 2004, pp. 38–43.

[116] J. Fortuny-Guasch, “A fast and accurate far-field pseudopolar format radar imaging algorithm,” *Geoscience and Remote Sensing, IEEE Transactions on*, vol. 47, no. 4, pp. 1187–1196, April 2009.

[117] B. Fan, Y. Qin, P. You, and H. Wang, “An improved PFA with aperture accommodation for widefield spotlight SAR imaging,” *Geoscience and Remote Sensing Letters, IEEE*, vol. 12, no. 1, pp. 3–7, Jan 2015.

[118] R. Linnehan, M. Yasuda, and A. Doerry, “An efficient means to mitigate wavefront curvature effects in polar format processed SAR imagery,” in *SPIE Defense, Security, and Sensing*. International Society for Optics and Photonics, 2012, pp. 83 611N–83 611N.

[119] D. North, “An analysis of the factors which determine signal/noise discrimination in pulsed-carrier systems,” *Proceedings of the IEEE*, vol. 51, no. 7, pp. 1016–1027, July 1963.

[120] J. W. Cooley and J. W. Tukey, “An algorithm for the machine calculation of complex fourier series,” *Mathematics of computation*, vol. 19, no. 90, pp. 297–301, 1965.

[121] J. Marsden, A. Tromba, and A. Weinstein, *Basic multivariable calculus*. Springer-Verlag, 1993.

[122] Q. Wang and W. Lei, “A novel NUSS-FFT SAR imaging algorithm of non-uniform spatial sampling data,” in *Mechanic Automation and Control Engineering (MACE), 2011 Second International Conference on*. IEEE, 2011, pp. 3795–3798.

[123] M. Scherreik, L. A. Gorham, and B. D. Rigling, “New phase error corrections for polar format algorithm with squinted SAR,” *IEEE Transactions on Aerospace and Electronic Systems*, 2015, in public release approval, to be submitted.